GEOPHYSICS, VOL. 80, NO. 4 (JULY-AUGUST 2015); P. D363–D383, 21 FIGS., 3 TABLES.
10.1190/GEO2014-0535.1

Measurements of elastic and electrical properties of an unconventional organic shale under differential loading

W. F. Woodruff[1], A. Revil[2], M. Prasad[3], and C. Torres-Verdín[4]

ABSTRACT

We have developed an experimental approach to simultaneously measure the stress dependence of ultrasonic wave velocities at 1 MHz, and therefore the components of the undrained elastic stiffness tensor, as well as the components of the complex conductivity tensor in the frequency range from 100 mHz to 10 Hz. We performed the experiments on a cylindrical core sample from the Haynesville Formation (porosity of approximately 0.08, bound water excluded, and clay content, mostly illite, approximately 30–40 wt%). We performed experiments under controlled confining and pore fluid pressures, achieving differential pressure states representative of autochthonous reservoir conditions. Directional measurements were made using independent acquisition arrays (piezoelectric crystals and nonpolarizing electrodes) distributed azimuthally on the core sample external surface, the bedding plane being along the axis of the cylindrical core sample. Ultrasonic waveforms were recorded on a high-resolution oscilloscope, and complex impedance spectra were recorded with a four-electrode acquisition system using an impedance meter with precision of 0.1 mrad. Experiments were repeated under drained and undrained conditions, over loading and unloading sequences for fully water-saturated conditions. Measurements show strong stress dependence on ultrasonic and complex conductivity measurements, which can be ascribed to the opening and closing of cracks within the samples. The data were used to estimate the anisotropic electrical and elastic effective pressure coefficients of the core sample, resulting in effective stress coefficients smaller than one for both elastic and electrical properties. These effective stress coefficients were also smaller for the electrical and acoustic properties once the cracks have closed. The anisotropy ratio for the components of the complex conductivity tensor was on the order of 30, whereas it was only 2 for the compressional components of the stiffness tensor (C_{11}/C_{33}).

INTRODUCTION

The role of rock mechanics and the connection between different petrophysical measurements (permeability, mechanical, and electromagnetic properties) and the state of stress of oil and gas shales is gaining increasing importance in the multiscale exploration, characterization, and production of unconventional oil and gas reservoirs (Yang and Zhang, 2002; Kachanov and Sevostianov, 2005; Josh et al., 2012). Such reservoirs are characterized by low porosities, very low permeability ($\ll$1 mD), and the presence of kerogen. The goal of these studies is to understand the anisotropic effects of local and regional stresses acting in situ on these formations, the existence of sweet spots that can be produced at affordable costs, and the evolution of the transport properties during production (Vernik and Liu, 1997; Johansen et al., 2004; Chalmers et al., 2012). Knowledge of the electromagnetic properties (conductivity and permittivity) of oil shales is also required to determine the efficiency of radio frequency dielectric heating (Sweeney et al., 2007) or to interpret time-lapse crosswell electromagnetic imaging (MacLennan et al., 2014).

Ultrasonic and electrical measurements can be used to assess the effect of the stress state and describe the poroelastic (undrained) response of a core sample. The study of the propagation of seismic waves in fluid-saturated porous media is pioneered by Frenkel

Manuscript received by the Editor 15 November 2014; revised manuscript received 9 February 2015; published online 26 May 2015.
[1]Colorado School of Mines, Department of Geophysics, Golden, Colorado, USA. E-mail: wfwoodruff@gmail.com; mprasad@mines.edu.
[2]Colorado School of Mines, Department of Geophysics, Golden, Colorado, USA and Université Savoie Mont Blanc, ISTerre, CNRS, UMR CNRS, Le Bourget du Lac, France. E-mail: arevil@mines.edu
[3]Colorado School of Mines, Department of Geophysics, and Department of Petroleum Engineering, Golden, Colorado, USA.
[4]University of Texas at Austin, Department of Petroleum and Geosystems Engineering, Austin, Texas, USA. E-mail: cverdin@austin.utexas.edu.

(1944) and Biot (1955, 1956, 1962). Extension of the poroelastic theory to anisotropic media can be found in Carroll (1979) and Cheng (1997). In shales and mudstones, clay and kerogen contents and the effect of textural anisotropy are expected to impact the measured P- and S-wave velocities (Prasad et al., 2011) and the corresponding components of the undrained stiffness tensor.

The complex electrical conductivity tensor of oil and gas shales is modeled by Revil et al. (2013), and a validation of this model is discussed by Woodruff et al. (2014) using a broad data set of experimental measurements. Other recent works have successfully characterized the electrical anisotropy of laboratory sandstone samples at elevated pressures (North et al., 2013). In the case of acoustic and electrical measurements, oil and gas shales can be treated as transversely isotropic (TI) materials with the plane of isotropy corresponding to the foliation plane.

Advances have been made studying the joint characterization of effective electrical and elastic properties of sandstones in the laboratory (e.g., Han et al., 2011a, 2011b). However, in the context of the production of unconventional reservoirs, the response of the anisotropic acoustic and electrical properties to differential stress levels in drained and undrained conditions remains poorly understood (Passey et al., 2010, Kuila et al., 2014). To study the corresponding effects of the mechanical response of shales, we have developed a new measurement protocol incorporating the simultaneous acquisition of ultrasonic and spectral-induced polarization data sets on a core sample of gas shale (Haynesville gas shale), characterized by transverse isotropy (Woodruff et al., 2014). For transport properties, it is usually possible to define an effective stress law with an effective stress coefficient (e.g., Coyner, 1984; Bernabé, 1987). Our goal is to study the effective stress coefficient for these properties, which are measured simultaneously for the first time on the same core sample and to look for the effect of the closure of the cracks on the effective stress response.

BACKGROUND

Effective stress equations

In the context of porous materials with a Newtonian pore fluid and a linear elastic isotropic skeleton, the effective pressure of poroelasticity $P*$ (Pa) is given by

$$P* = P_c - \alpha P_p, \tag{1}$$

where P_c (in pascal [Pa]) defines the confining stress, P_p (in Pa) is the pore fluid pressure, and α (dimensionless) denotes the Biot coefficient, which obeys $0 \le \alpha \le 1$. In a practical sense, α separates the compressibility of a composite solid (rock) from the compressibility of its constituents (minerals). In the linear poroelastic framework, the Biot coefficient of an isotropic material is given by $\alpha = 1 - K/K_S \le 1$, where K is the static bulk modulus of the porous material in drained conditions (the frame bulk modulus) and K_s denotes the static bulk modulus of the solid phase (Biot and Willis, 1957). In soils, where the compressibility of the skeleton is much smaller than the compressibility of the solid grains, the Biot coefficient can approach unity (de Boer and Ehlers, 1990). On the other hand, in very stiff rocks (e.g., crystalline rocks), α can be close to zero. In anisotropic formations, Biot's coefficient is a second-rank symmetric tensor (e.g., Giot et al., 2012).

It is also customary to introduce effective stress laws for transport properties (Todd and Simmons, 1972; Coyner, 1984; Bernabé, 1987). These laws involve effective stress coefficients that are not necessarily similar to the effective stress coefficient defined above. In other words, the effective stress coefficient may be different for different petrophysical properties of porous media such as electrical conductivity, permeability, and mechanical/elastic properties (Coyner, 1984; Bernabé, 1987). We note that extraction of effective stress coefficients from specific physical property measurement is based on the sensitivity of that property to the compressibility contrast. The effective stress state for a given rock and the effective stress coefficient α is also stress dependent as compressibility changes with stress (e.g., Ghabezloo et al., 2008).

Our goal is to gain better insight regarding the effective stress coefficient for the undrained stiffness and complex conductivity tensors of a TI gas shale. The elastic and electrical properties can be measured at various differential pressure states to obtain the changes of a measured response with respect to an effective stress law. Todd and Simmons (1972) show that the effective stress coefficient for a given physical property χ can be estimated as (see Appendix A)

$$\alpha_\chi = 1 - \frac{\left.\frac{\partial \chi}{\partial P_p}\right|_{P_d}}{\left.\frac{\partial \chi}{\partial P_d}\right|_{P_p}}. \tag{2}$$

In the present work, we will apply equation 2 to the components of both the undrained stiffness and complex conductivity tensors.

Stiffness elastic tensor of transverse isotropic media

In an anisotropic porous material such as gas shale, the poroelastic equations in drained conditions can be written in incremental form as (e.g., Giot et al., 2012),

$$d\mathbf{\Sigma} = \mathbf{C} : d\boldsymbol{\epsilon} - \mathbf{A} dP_p \tag{3}$$

and

$$dm = \rho_f \left[\mathbf{A} : d\boldsymbol{\epsilon} + \left(\frac{1}{M} + \frac{\phi}{K_f} \right) dP_p \right], \tag{4}$$

where M_ϕ denotes the solid Biot modulus; ϕ denotes the (Lagrangian) porosity; m (kg m^{-3}) denotes the pore water mass exchanged between the core sample and the reservoirs; K_f (Pa) and ρ_f (kg m^{-3}) denote the bulk modulus and mass density of the pore fluid, respectively; $\mathbf{\Sigma}$ (Pa) denotes the second-rank stress tensor; $\boldsymbol{\epsilon}$ (dimensionless) is the second-rank strain tensor; and finally $\mathbf{C}$ (components in Pa) denotes the fourth-rank (drained) stiffness elastic tensor. The confining pressure is defined by $P_c = -(1/3) Tr\mathbf{\Sigma}$ where Tr(.) denotes the trace of the matrix representation of the tensor. We note $\mathbf{e}_i$ ($i = 1, 2, 3$) the basis vectors of the Cartesian frame of reference, and we assume that (O, $\mathbf{e}_3$) will be the axis of symmetry, normal to the foliation or bedding plane of the material. In our case, this direction will be normal to the center line of the cylindrical core sample as discussed further below.

The stiffness tensor is related to its components C_{ijkl} by $C = \mathbf{C}_{ijkl} \mathbf{e}_i \otimes \mathbf{e}_j \otimes \mathbf{e}_k \otimes \mathbf{e}_l$ where $\mathbf{e}_i \cdot \mathbf{e}_j = \delta_{ij}$ where δ_{ij} is the

Kronecker delta, whereas $\mathbf{a} \otimes \mathbf{b}$ denotes the tensorial product between the two vectors $\mathbf{a}$ and $\mathbf{b}$. This stiffness tensor is characterized by two Young's coefficients E_1 and E_3, two Poisson coefficients ν_{12} and ν_{13}, and a shear modulus G_{13} (see, for instance, Giot et al., 2012). Assuming that the core sample is transverse isotropic, the second-rank Biot tensor $\mathbf{A}$ entering equations 3 and 4 is expressed as

$$\mathbf{A} = \alpha_1(\mathbf{e}_1 \otimes \mathbf{e}_1 + \mathbf{e}_2 \otimes \mathbf{e}_2) + \alpha_3 \mathbf{e}_3 \otimes \mathbf{e}_3. \tag{5}$$

Therefore, the matrix representation of this tensor is

$$\mathbf{A} = \begin{bmatrix} \alpha_1 & 0 & 0 \\ 0 & \alpha_1 & 0 \\ 0 & 0 & \alpha_3 \end{bmatrix}, \tag{6}$$

where α_1 and α_3 are the Biot coefficients in the bedding plane and in the transverse direction. The incremental change of porosity can be written as (e.g., Giot et al., 2012)

$$d\phi = \mathbf{A} : d\boldsymbol{\epsilon} + \frac{1}{M_\phi} dP_p. \tag{7}$$

Note, however, that equation 7 accounts only for the reversible change of porosity associated with the poroelastic deformation of the porous material. We will see that the deformation of the core sample in our experiments is characterized by a small component of irreversible deformation (damage).

The experiments that will be described below are made in the drained and undrained states. However, we will not try to measure the deformation of the sample or the mass of fluid exchanged between the sample and the reservoirs. Instead, we will measure the stiffness tensor using ultrasonic measurements. At a given compaction state, the ultrasonic measurements probe the undrained stiffness tensor of the material (i.e., the pore fluid has no time to flow in response to the stress solicitation associated with the passage of the seismic waves). In an undrained porous material, the mechanical constitutive equation corresponds to another form of Hooke's law, which is written in incremental form as

$$d\boldsymbol{\Sigma} = \mathbf{C}^u : \mathbf{d}\boldsymbol{\epsilon}, \tag{8}$$

where $\mathbf{C}^u$ denotes the fourth-rank undrained stiffness elastic tensor (with components C^u_{ijkl}). The relationships between the components of the undrained stiffness tensor and those of the drained stiffness tensor can be found in Cheng (1997) under the assumption that the macroscopic anisotropy is due to the arrangement of the pores and grains and not the anisotropy of the microfabric in the solid phase. Equation 8 can be written as $\boldsymbol{\Sigma}_i = C^u_{ij}\epsilon_j$ (with the Einstein convention) using the Voigt matrix representations (indices i and j) of the stiffness elastic tensor connecting the components Σ_{ij} of the stress tensor to the components ϵ_{kl} of the strain tensor of the solid phase (Backus, 1962). In the following, all the stiffness tensor components will be undrained components and we will drop the superscript "u" for simplicity.

In transverse isotropic materials where index 3 indicates the axis of symmetry, Hooke's law is given by

$$\begin{bmatrix} d\Sigma_1 \\ d\Sigma_2 \\ d\Sigma_3 \\ d\Sigma_4 \\ d\Sigma_5 \\ d\Sigma_6 \end{bmatrix} = \begin{bmatrix} C_{11} & C_{11}-2C_{66} & C_{13} & 0 & 0 & 0 \\ C_{11}-2C_{66} & C_{11} & C_{13} & 0 & 0 & 0 \\ C_{13} & C_{13} & C_{33} & 0 & 0 & 0 \\ 0 & 0 & 0 & C_{44} & 0 & 0 \\ 0 & 0 & 0 & 0 & C_{44} & 0 \\ 0 & 0 & 0 & 0 & 0 & C_{66} \end{bmatrix} \times \begin{bmatrix} d\varepsilon_1 \\ d\varepsilon_2 \\ d\varepsilon_3 \\ d\varepsilon_4 \\ d\varepsilon_5 \\ d\varepsilon_6 \end{bmatrix}. \tag{9}$$

The complex conductivity tensor

Oil and gas shales being anisotropic materials, their complex conductivity tensor is expected to be direction dependent. Very few works have investigated the complex conductivity of anisotropic materials (e.g., Zisser and Nover, 2009; Zisser et al., 2010; Revil et al., 2013; Woodruff et al., 2014) or have compared the anisotropy behavior of ultrasonic P-wave velocity and electrical conductivity (Louis et al., 2003). In water-saturated porous materials, the electrical constitutive equation of interest is the generalized ohm's law, which can be obtained from nonequilibrium thermodynamics and Ampères law as (Vinegar and Waxman, 1984)

$$\mathbf{J} = \boldsymbol{\sigma}* \cdot \mathbf{E}, \tag{10}$$

where $\mathbf{J}$ ($\mathrm{A\,m^{-2}}$) is the total current density, and $\mathbf{E}$ ($\mathrm{V\,m^{-1}}$) is the electric field. The complex conductivity tensor $\boldsymbol{\sigma}*$ is related to its complex-valued components σ^*_{ij} by $\boldsymbol{\sigma}* = \sigma^*_{ij}\mathbf{e}_i \otimes \mathbf{e}_j$ in $\mathrm{S\,m^{-1}}$) where $\mathbf{e}_i$ ($i = 1, 2, 3$) correspond to the basis vectors of the Cartesian frame of reference. Equation 10 can also integrate the displacement current, so, the complex conductivity can integrate dielectric effects such as Maxwell-Wagner polarization mechanisms (see Revil [2013a, 2013b] for further discussions).

Each component of the complex conductivity tensor is a complex number and can be written as

$$\sigma_{ij}* = \sigma'_{ij} + i\sigma''_{ij}, \tag{11}$$

where $i^2 = -1$ (i denotes the pure imaginary number). In a transverse isotropic material (with axis 3 being the axis of symmetry, normal to the foliation plane), the complex conductivity tensor is given by

$$\begin{aligned} \boldsymbol{\sigma}* = {} & (\sigma'_{11} + i\sigma''_{11})(\mathbf{e}_1 \otimes \mathbf{e}_1 + \mathbf{e}_2 \otimes \mathbf{e}_2) \\ & + (\sigma'_{33} + i\sigma''_{33})\mathbf{e}_3 \otimes \mathbf{e}_3, \end{aligned} \tag{12}$$

and therefore, the generalized ohm's law is given by

$$\begin{bmatrix} J_1 \\ J_2 \\ J_3 \end{bmatrix} = \begin{bmatrix} \sigma'_{11} + i\sigma''_{11} & 0 & 0 \\ 0 & \sigma'_{11} + i\sigma''_{11} & 0 \\ 0 & 0 & \sigma'_{33} + i\sigma''_{33} \end{bmatrix} \begin{bmatrix} E_1 \\ E_2 \\ E_3 \end{bmatrix}, \tag{13}$$

in a Cartesian framework aligned with the eigenvectors of the complex conductivity tensor (axis 3 normal to the foliation plane).

The components σ'_{ij} represent the real (in-phase) components of the complex conductivity tensor, and these components describe electromigration phenomena affecting the charge carriers. Electromigration occurs in the bulk pore space and in the electrical double layer coating the surface of the grains. This electrical double layer comprises the Stern layer of counterions sorbed on the surface of the grains and the diffuse layer in which the counterions and coions are bound to the mineral surface through Coulombic interactions. The components σ''_{ij} denote the imaginary (out-of-phase or quadrature) components. These components describe the polarization or capacitive effect of the core sample, or in other words, the reversible storage of electrical charges in the porous material. In addition, these quadrature components can be affected by dielectric polarization phenomena such as the Maxwell-Wagner or high-frequency polarization effects (see Revil, 2013a, 2013b).

Revil (2013a) develops a complex conductivity model obtained by volume-averaging the Nernst-Planck equation in isotropic porous media. At high porosities, this model is consistent with the Waxman and Smits (1968) equation of electrical conductivity and the Vinegar and Waxman's (1984) model of polarization. That said, Revil's (2013a) model seems more accurate at low porosities (see Woodruff et al., 2014). In this model, the quadrature conductivity is mostly controlled by the polarization of the Stern layer of counterions. Neglecting Maxwell-Wagner polarization, Revil et al. (2013) extend this model to the anisotropic case and provide analytical expressions describing the in-phase and quadrature components of the complex conductivity tensor as

$$\sigma'_{ij} \approx F_{ij}\sigma_w + T_{ij}\rho_S[\beta_{(+)}(1-f) + \beta^S_{(+)}f]\mathrm{CEC} \tag{14}$$

and

$$\sigma''_{ij} = T_{ij}\rho_S\beta^S_{(+)}f\,\mathrm{CEC}, \tag{15}$$

respectively. In the above equations, F_{ij} denotes the components of the (symmetric second rank) conductivity formation factor tensor for the conductivity $\mathbf{F}$, and T_{ij} denotes the components of the (symmetric second rank) tortuosity tensor of the pore space $\mathbf{T}$. For transverse isotropic materials, these two tensors are defined as

$$\mathbf{F} = \frac{1}{F_1}(\mathbf{e}_1 \otimes \mathbf{e}_1 + \mathbf{e}_2 \otimes \mathbf{e}_2) + \frac{1}{F_3}\mathbf{e}_3 \otimes \mathbf{e}_3, \tag{16}$$

$$\mathbf{T} = \frac{1}{\tau_1}(\mathbf{e}_1 \otimes \mathbf{e}_1 + \mathbf{e}_2 \otimes \mathbf{e}_2) + \frac{1}{\tau_3}\mathbf{e}_3 \otimes \mathbf{e}_3, \tag{17}$$

and $F_1 = \tau_1/\phi$ and $F_3 = \tau_3/\phi$. The terms $F_{1,3}$ are analogous to the classical (resistivity) formation factors (>1) whereas the terms $\tau_{1,3}$ are analogous to the classical tortuosities (>1) of the pore space in the foliation plane (directions 1 and 2) and normal to the foliation plane (direction 3).

The partition coefficient f entering equations 14 and 15 (dimensionless, typically in the range 0.85 to 0.99; see Revil, 2012, 2013a, 2013b), denotes the fraction of counterions in the Stern layer, ρ_S denotes the mass density of the solid phase (typically 2650 ± 50 kg m^{-3} for the crystalline framework of clay minerals), σ_w (S m^{-1}) denotes the conductivity of the pore water, and CEC (see equations 14 and 15) corresponds to the cation exchange capacity of the material (expressed in C kg^{-1}). The parameter $\beta_{(+)}$ denotes the mobility of counterions in the electrical diffuse layer, whereas $\beta^S_{(+)}$ denotes the mobility of counterions in the Stern layer (both are expressed in m^2 s^{-1} V^{-1}). For clay minerals, the mobility of counterions in the diffuse layer is equal to the mobility of the same counterions in bulk pore water (e.g., $\beta_{(+)}(\mathrm{Na}^+, 25°\mathrm{C}) = 5.2 \times 10^{-8}$ m^2 s^{-1} V^{-1}; see Revil, 2012, 2013a, 2013b) whereas the mobility of the counterions in the Stern layer is substantially smaller with $\beta^S_{(+)}(25°\mathrm{C}, \mathrm{Na}^+) = 1.5 \times 10^{-10}$ m^2 s^{-1} V^{-1} for clay minerals (Revil, 2012, 2013a, 2013b; Revil et al., 2013).

Stiffness tensor and mechanical compaction

Pictures of the core sample used in this study are shown in Figures 1 and 2, and the position of the foliation plane with respect to the sample axis is shown in Figures 1 and 3 (the 90° angle direction is normal to bedding). The components of the stiffness elastic tensor can be derived from azimuthal velocities (as measured from the isotropic reference plane) of the compressional velocity V_P, and the fast horizontal and vertical S-wave velocities v_{SH0} and V_{S90}, respectively (see Figure 3). The six independent (undrained) stiffness coefficients in equation 9 can be obtained from five directional velocity measurements (e.g., Hornby, 1998) namely,

$$C_{11} = \rho V^2_{\mathrm{P0}}, \tag{18}$$

$$C_{33} = \rho V^2_{\mathrm{P90}}, \tag{19}$$

$$C_{44} = \rho V^2_{\mathrm{S90}}, \tag{20}$$

$$C_{66} = \rho V^2_{\mathrm{SH0}}, \tag{21}$$

and

$$C_{12} = \rho(V^2_{\mathrm{P0}} - V^2_{\mathrm{SH0}}) = C_{11} - 2C_{66}, \tag{22}$$

where the vertical translational component is obtained from C_{11}, C_{33}, C_{44}, and an off-axis P- or S-velocity measurement (typically at 45° incidence to the foliation plane)

$$C_{13} = -C_{44} + m\sqrt{(C_{11} + C_{44} - 2\rho V^2_{45})(C_{33} + C_{44} - 2\rho V^2_{45})}, \tag{23}$$

taking $m = -1$ for off-axis P-velocity and $m = 1$ if the off-axis shear velocity is used. In these equations, ρ (kg m^{-3}) denotes the mass density of the material (2450 kg m^{-3} from Figures 1 and 2 of Jiang and Spikes, 2013) and where the velocity subscripts indicate the wave type (subscripts P and S denote the compressional and shear waves, respectively), and direction (subscripts 0 and 90 denote the horizontal and vertically propagating waves; see Figure 3).

The vertical S-wave and the horizontal S-wave polarized in the vertical plane V_{SV0} are assumed equal and are denoted by V_{S90}. Shear sources and the measured arrivals are polarized, thus allowing for the isolated measurement of the velocities along each of the independent directions defined by the stiffness tensor. For a differential pressure increment and therefore an associated compaction increment of the material, the effective stress laws for the stiffness coefficients are discussed in Appendix B.

As previously emphasized, the complex conductivity and ultrasonic wave velocities are both dependent on the effective pressure applied to the porous medium. This pressure state is in turn related to the consolidation of the material through the compaction of the pore space and the deformation of minerals. The nature of the mechanical behavior of the microstructure in rocks is complex (e.g., deformation and elongation of pores and micropores, closure of the cracks, realignment of platy minerals, irreversible creep, or pore collapse to list a few). Nevertheless, the macroscopic effect of mechanical compaction in the quasilinear elastic regime can be described according to changes in the bulk textural properties used to define the elastic and electric properties in the preceding sections. We will also assume that the deviations between the electric and elastic tensor eigenvectors are small and can be neglected.

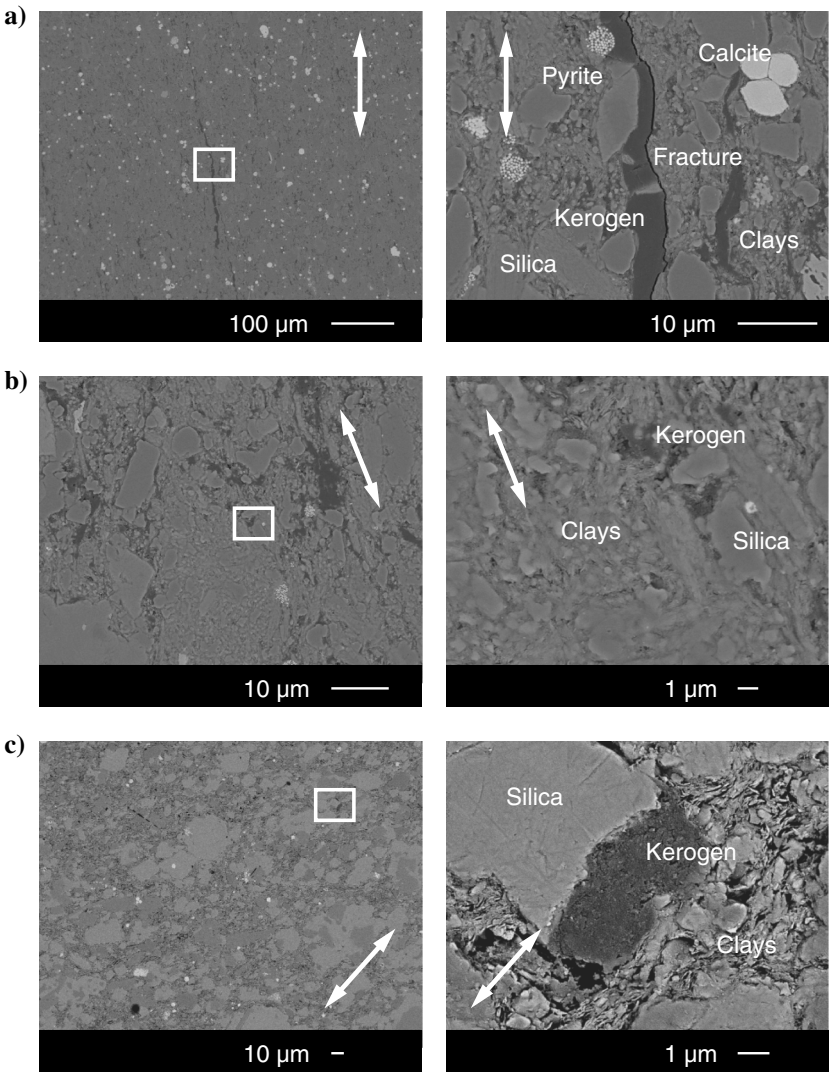

Figure 1. Photomicrographs of the Haynesville gas shale showing its microstructure. We generalized the textural properties of the Haynesville core according to the microscopic features that have the greatest impact on the ultrasonic and spectral-induced polarization measurements. (a) Microscopic decompression fractures, (b) preferential alignment of clay minerals, and (c) heterogeneous pore network ranging from intergranular porosity, mesoporosity, and microporosity in the clay laminations, and kerogen porosity. In each set of images, the right panel shows the area outlined in white in the left image at 10× magnification.

Complex conductivity tensor and mechanical compaction

In anisotropic conditions, we obtain the components of the two textural tensors **F** and **T** from the in-phase and quadrature conductivities from equations 14 and 15, as follows. The components of the formation factor tensor can be obtained as

$$F_{ij} = \sigma_w^{-1}\left[\sigma'_{ij} - \sigma''_{ij}\left(1 - \frac{\sigma_d}{\sigma_S}\right)\right], \qquad (24)$$

whereas the components of the tortuosity tensor are obtained according to

$$T_{ij} = \frac{\sigma''_{ij}}{\sigma_S}. \qquad (25)$$

In equations 24 and 25, the conductivities of the Stern and diffuse layers are given by $\sigma_S = \rho_S \beta^S_{(+)} f\mathrm{CEC}$ and $\sigma_d = \rho_S \beta_{(+)}(1-f)\mathrm{CEC}$ and $\sigma_d/\sigma_S = \beta_{(+)}(1-f)/[\beta^S_{(+)} f] \approx 2.22$ (see equations 14 and 15). The CEC of the Haynesville Formation is between 13.9 and 3.6 meq/100 g (Breeden et al. [2011], equivalent to 13,000 to 3400 $\mathrm{C\,kg^{-1}}$). Kuila (2013) measure the CEC of several samples from the Haynesville Formation. His data are shown in Figure 4 together with the data from Breeden et al. (2011). The linear trend between the CEC and the clay content shown in Figure 4 will be used to estimate the CEC from the clay content of our core sample, which is done in the next section.

DESCRIPTION OF THE EXPERIMENTS

We used a cylindrical plug (sample H251; see Table 1 for its mineralogical composition and Table 2 for the porosity) from a whole core specimen of the Haynesville shale formation. This sample was encased in a jacket designed to perform joint acoustic/electrical measurements under effective hydrostatic load and saturated with a pore fluid solution balanced with the mineralogy of the sample. Equilibrium molar concentrations were 1.157×10^{-3} (CO_2(aq), H_2CO_3, HCO_3, and CO_3^{2-}), 5.8×10^{-4} (Ca), and 7.515×10^{-5} (Si) (Woodruff et al., 2014). The sample was dried under low vacuum and saturated in a pressurized low-salinity mineral

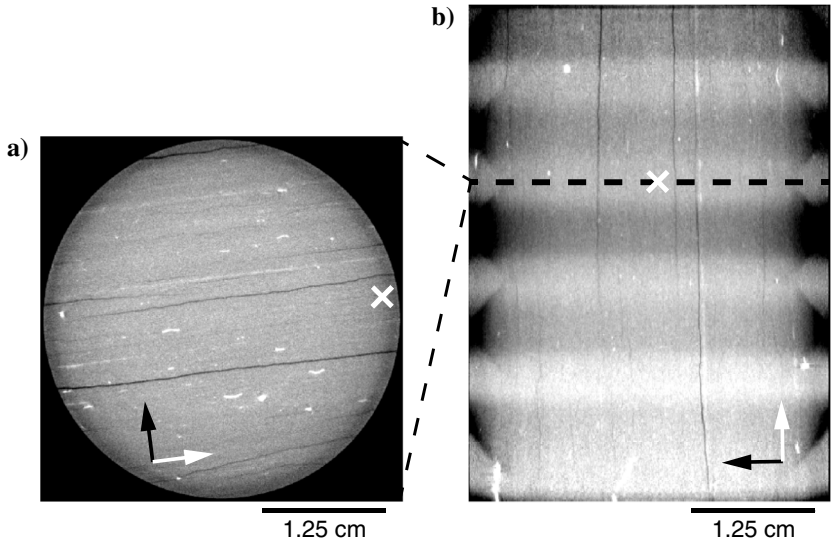

Figure 2. Vertical and horizontal slices obtained from X-ray tomograms depicting the pervasive decompression fracture distribution in the core sample. Fractures are aligned predominantly in the foliation plane, but they exhibit some conchoidal features. The fracture networks have pronounced effects on ultrasonic and electrical measurements. Dashed lines indicate where the horizontal slice intersects the (b) vertical slice. The white X's collocate the images azimuthally, the white arrows are oriented in-plane, and the black arrows are transverse to the fracture plane. Because the cracks are in the foliation plane, they do not affect the transverse anisotropy of the material. Figure is modified from Woodruff et al. (2014).

slurry prepared from a piece of the Haynesville sample. The saturation state was monitored over several months through gravimetric analysis until fully saturated. A detailed description of the core preparation protocols (machining, fluid synthesis, and saturation), laboratory equipment, and measurement protocols is provided in Woodruff et al. (2014), and the readers are directed to that paper for the details.

We measured the ultrasonic velocity and complex impedance of the sample under controlled differential loading conditions. The pore and confining pressures are modulated with syringe pumps (Teledyne ISCO model 100DM), enabling precise control of the differential stress ranging from 0 to 34.5 MPa at increments of 3.45 MPa per stage. Drained experiments were performed on the saturated sample with a drained pore fluid line, using a gradual pressure ramp of 3.5 kPa per minute and a stabilization period at each stage. Undrained experiments were performed with controlled pore line pressure. An equilibration time of 30 min was determined by comparing the time response of ultrasonic waveforms, which allowed for adequate stabilization of the sample while not being prohibitive for the length of these experiments. The acoustic velocity measurements were acquired at 1 MHz (ultrasonic frequency) whereas the electrical impedance spectroscopic data were acquired in the frequency range of 50 mHz to 1000 Hz. The ultrasonic frequency 1 MHz is used to generate wavelengths compatible with the laboratory scale of the core sample whereas the low frequency of the complex conductivity measurements is justified by the occurrence of electrical double-layer polarization processes at

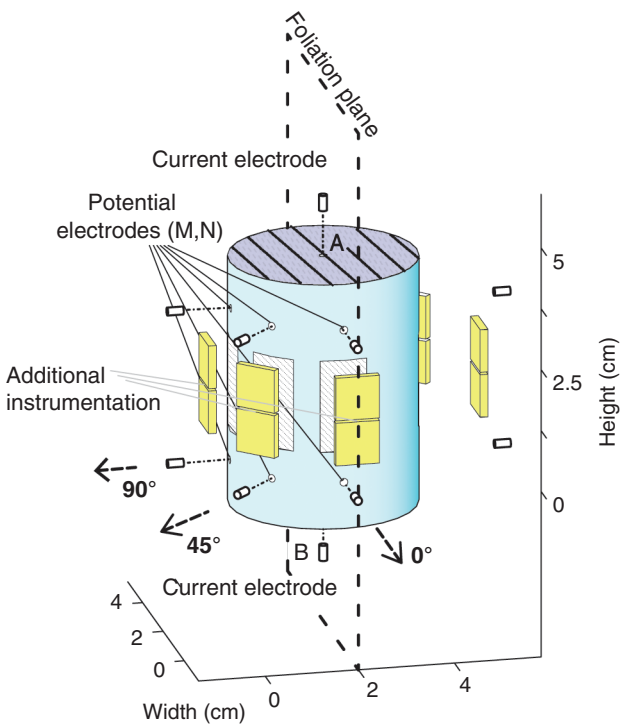

Figure 3. Azimuthal array for anisotropic spectral-induced polarization measurements. Electrodes are distributed radially about the core (the axis is coincident with the isotropic plane) to sample the change in electrical potential field distribution over the surface. Impedance measurements can be inverted for the full electrical tensor and the rotation eigenvectors. Axes 1 and 2 are along the bedding/foliation plane, whereas axis 3 is normal to the bedding/foliation plane.

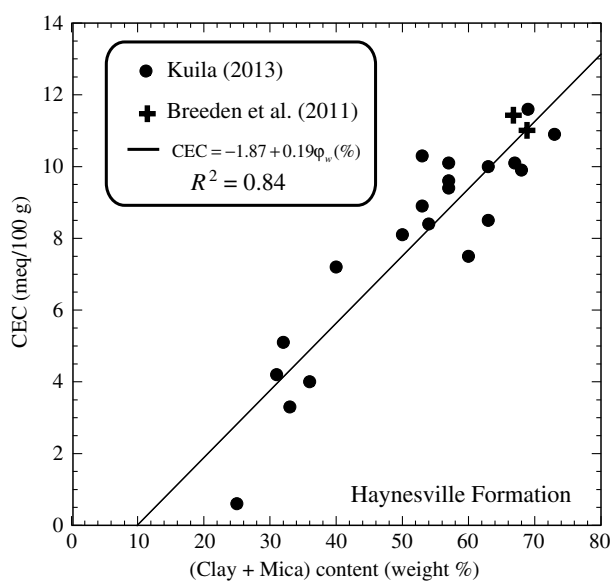

Figure 4. Relationship between the clay content and the cation exchange capacity of core samples from the Haynesville Formation (data from Breeden et al. [2011] and Kuila, 2013). Meq means milliequivalent and ϕ_w (%) expresses the clay content in weight percent.

this frequency range (Revil et al., 2013; Woodruff et al., 2014). At each pressure stage, the directional group velocities are recorded as the picked first break of the waveforms (Prasad and Manghnani, 1997; Dewhurst and Siggins, 2006; Nadri et al., 2012) to estimate the elastic modulus components, and the complex voltages (impedance magnitude and phase) are measured to obtain the components of the complex conductivity (Zimmerman, 2008a).

Description of the Haynesville core sample

The Haynesville Formation is located in the Texas-Louisiana Salt Basin. Haynesville shales are generally characterized as silty, argillaceous or calcareous mudstones, and dolomitic mudstones and dolostones with a strong vertical transverse anisotropy (Horne et al., 2012; Jiang and Spikes, 2013). The formation varies compositionally, depending on the position in the stratigraphic column. In situ sampling indicates clay content of 30% (±10%), 15% (±10%) calcite, and 4% (±3%) total organic content (TOC), by mass. Chalmers et al. (2012) report a TOC of 4.2% (type II kerogen distributed in the rock). Chalmers et al. (2012) report a mean pore diameter of 4.9 nm, a porosity of 6.2%, and a clay content of 44% in weight (essentially illite and some chlorite). Elgmati et al. (2011) report a mean pore size of 6.5 nm (Hg-porosimetry), a porosity of 10.3%,, and a permeability of 1.4×10^{-4} mD.

The texture of the Haynesville mudstone exhibits laminated fabrics ranging on both the scale of the mineral foliations, as well as that of the depositional bedding planes. Environmental scanning electron microscope (SEM) images taken from the Haynesville core confirm the microstructure visible on the surface of the core (Figure 1), showing clay laminations, mineral heterogeneity, kerogen distribution, and the presence of cracks.

Recovered Haynesville samples are fissile and exhibit usually decompressional stress-related cracks. These cracks are shown by x-ray computerized axial tomography to be predominantly aligned in the plane of mineral foliations (Figure 2), some of them traversing the entire core with some conchoidal character. As we will show below, such fractures have pronounced effects on the ultrasonic and complex conductivity measurements, exhibiting characteristic changes resulting from the closure of the cracks. Due to the relatively ubiquitous volume fraction of clay and homogeneous water saturation, porosity and density are also tied closely to the calcite distribution (Skelt, 2011).

The core sample was machined to improve the accuracy of sample dimensioning and sensor placement; bulk samples were well characterized prior to machining through standard core analysis, X-ray diffraction, computed tomography imaging, SEM imaging, as well as ultrasonic measurements to determine the baseline material properties. The dry sample was evacuated under vacuum and pressure saturated with an equilibrium solution prepared in balance with the characterized mineralogy of the sample (see Woodruff et al. [2014] for a detailed description of the saturation procedure). It was pressurized at 10.34 MPa for a period of 72 h, and it was left to equilibrate within a saturated jacket for an additional 120 days (flooded with a drained, saturated pore line, at 0 Pa).

For the sample investigated in the present work, a clay content of 30% yields a CEC value of 3.8 meq/100 g (3700 $\mathrm{C\,kg^{-1}}$) according to the relationship determined in Figure 4. The conductivity of the equilibrium solution was determined with PHREEQC (http://wwwbrr.cr.usgs.gov/projects/GWC_coupled/PHREEQC) to be 88 $\mu\mathrm{m\,cm^{-1}}$ (~0.0088 $\mathrm{S\,m^{-1}}$). The equilibration time was typically 12–24 h (see Woodruff et al., 2014). It follows that using the following values, $\sigma_w = 0.01\ \mathrm{S\,m^{-1}}$, $\beta_{(+)} = 5 \times 10^{-8}\ \mathrm{m^2\,s^{-1}\,V^{-1}}$ (mobility of sodium in water at 25°C), $\beta^S_{(+)} = 0.05\beta_{(+)}$ (default value for the mobility of sodium in the Stern layer at 25; see Revil, 2013a), and the default value of the partition coefficient $f = 0.90$ (see Revil, 2013b), we obtain $\sigma_S = 0.0221\ \mathrm{S\,m^{-1}}$ and $\sigma_d = 0.049\ \mathrm{S\,m^{-1}}$. This indicates very clearly that applying Archie's law for the electrical conductivity without a correction from the surface conduction is not an appropriate choice because surface conductivity appears as a very important component of the overall conductivity of the porous material. Note that the independent measurements of the formation factor (from the in-phase and quadrature conductivities) and the tortuosity tensor (from the quadrature conductivity alone) can also be used to estimate the porosity at a given compaction state. At the end of this paper, we will try to perform such a computation for different differential pressures.

Table 1. Representative mineralogy of the Haynesville samples from quantitative X-ray diffraction analysis. The median, maximum, and median mass fractions (in percent) are provided in different columns.

Mineral fraction (wt%)	Median	Maximum	Minimum
2:1 clay (M)	45.0	57.0	26.0
Quartz	28.0	31.0	13.0
Calcite	14.0	38.0	6.0
Plagioclase	5.0	11.0	3.0
TOC	3.5	6.3	2.5
Chlorite	2.0	4.0	0.6
Pyrite	2.0	7.0	1.0

Table 2. Haynesville core sample description from standard core analysis including the mass fraction of the predominant mineralogy and porosity as obtained from pulverized samples (Gas Research Institute [GRI] method) and from Archimedes' method (water immersion porosity [WIP], ϕ; see Kuila, 2013; Kuila et al., 2014). Additional petrophysical studies of downhole measurements are consistent with these observations. TOC denotes total organic content.

Sample	Quartz (wt%)	Carbonate (wt%)	Sum clay (wt%)	TOC (wt%)	ϕ (GRI)	ϕ (WIP)
H251	21	32.5	29.6	5.38	0.087	0.041

Jacketed core assembly

A jacket was designed to encase the sample and the affixed sensors, as well as to provide a closed pressure system. The core assembly allows for anisotropic characterization of cylindrical plugs with a height of 51 mm, and diameter 38 mm, with an axis aligned in the foliation plane, corresponding to the isotropic plane of symmetry. It was designed for the measurement of electrical potentials and acoustic wave velocities, using three separate azimuthal arrays distributed about the circumference of the sample (see Figure 3).

The jacketed assembly incorporates 2.0-mm sintered Ag/AgCl pellet electrocardiography electrodes and lead zirconate titanate (PZT) ceramic piezoelectric crystals for joint acquisition of spectral-induced polarization and ultrasonic measurements. These sensors were arranged azimuthally about the core axis. Figures 3 and 5 depict the core, sample jacket, acquisition geometry, and sensor locations with respect to the foliation plane of the core sample. Prior to placing the sensors, additional precision machining was performed to prepare the surface of the sample for instrumentation (14 Ag/AgCl electrodes; 12 PZT crystals). We drill 2.0-mm diameter sockets in the center of the top and bottom surfaces to house the current electrodes, and pairs of sockets radially about the core at precise angles of 0°, 45°, and 90° relative to the foliation plane (0°, demarking the isotropic plane, was estimated prior to machining; see Figure 3).

For the ultrasonic array, we machine parallel surfaces for the ultrasonic wave propagation experiments along the same azimuths. Electrodes are separated by 31.75 mm. The cylindrical surface is painted to electrically insulate the sample; we have found Revlon, clear coat and quick-drying nail polish to have favorable insulating properties, with good resistance to moisture and immersion in water. The top and bottom surfaces as well as the inner surfaces of the electrode sockets are left clean. The end caps are affixed, and a bead of epoxy is placed along the contacting edges to seal the inner and outer portions of the assembly and prevent leakage around the outside of the sample. Sensors are coupled to the sample with conducting silver epoxy, and leads are soldered to feedthroughs in the end cap. The exterior of the sample, including the sensors and lead wires, is encased in a highly compliant resin.

Measurement systems

A steel pressure vessel filled with a low-compressibility, low-conductivity oil is used to apply hydrostatic pressure to confine the sample under a prescribed load and electrically insulate the sensor leads on the immersed sample. Two Teledyne ISCO model 100DM syringe pumps are used to modulate the opposed confining pressure P_c (MPa) in the vessel and pore line pressure P_p (MPa) inside the sample jacket.

A Tektronix TDX 3014C oscilloscope is used to acquire the acoustic waveforms. The acoustic source is controlled by an electronic pulser, which modulates the voltage (300 V at full range) and pulse width of the electrical current in the piezoelectric crystal exciting a resonant frequency of 1 MHz in the crystal. We measure the traveltime t (μs) between the pulse and the source and receiver crystals for P- and S-waves. Velocity is calculated as $v = 2r/t$ (km s^{-1}), where $r = 3.81$ cm is the radius of the core sample. Data are acquired and traveltimes for the acoustic waves are picked using Spec4Win software with an error of less than 1% for the P-wave velocity (Prasad and Manghnani, 1997) and less than 4% for the S-wave velocity. In unconsolidated sands, evaluates velocity errors to be 2% for V_P and 4% for V_S. The waveforms for our experiment (Figure 6) allow us to anticipate velocity errors of 1% for V_P and 1%–3% for V_S with the lower number for shear velocity in the bedding plane and at lower pressures.

Regarding the determination of the complex conductivity, we use the ultrasensitive impedance meter designed by Egon Zimmermann (Zimmermann et al., 2008a, 2008b) instrumented with sintered Ag/AgCl electrochemical (nonpolarizing) electrodes and configured according to the protocols published recently by Woodruff et al. (2014). The system comprises a four-channel acquisition array and nominal frequency range of 1 mHz to 45 kHz. Figure 7a shows a sketch of the spectral-induced polarization acquisition system characterized by a sensitivity of 0.1 mrad in-phase shift. A current I_0 is excited in the sample by an applied voltage U_1 between two stimulus electrodes 1 and 4 (or A and B), located at the top and bottom faces of the core sample (Figures 3 and 5). We approximate the resistance in the medium as a linear circuit using $Z_m = U_m/I$, where $Z_m \approx Z_x$ denotes the true impedance in ohms, $U_m \approx U_x$ denotes the potential difference between the Ag/AgCl measuring electrodes 2 and 3 (voltage electrodes M and N) in volts (V), and I is the electrical current in amperes. For shales, in the voltage range 1–10 V, the

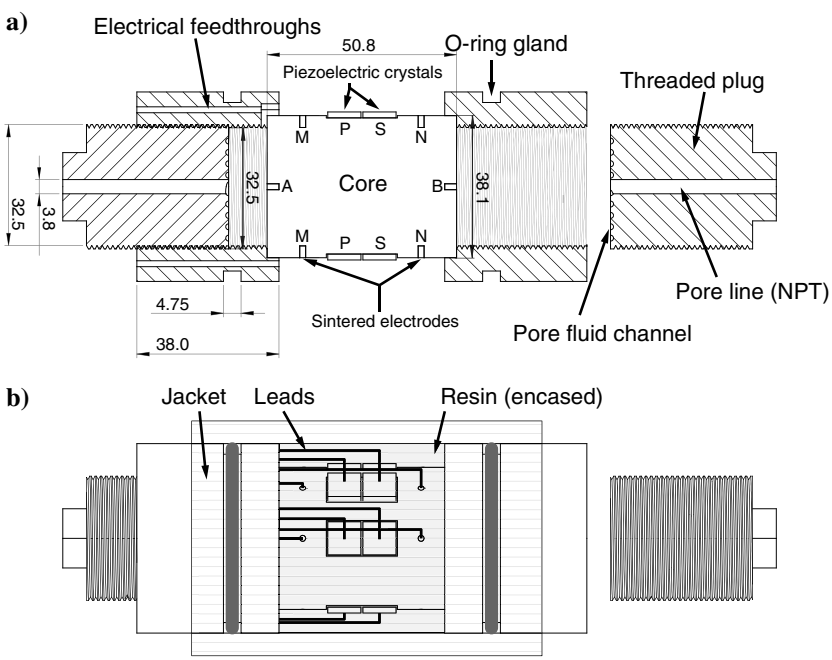

Figure 5. Sketch of the end cap for the jacketed core assembly. Feedthroughs are distributed radially in the outer ring and the removable center plug is threaded for the NPT pore line fittings. The removable plug enables saturation of the sample after the sample is encased in the jacket. The dimensions (in millimeters) of A and B denote the current electrodes whereas M and N denote the potential electrodes.

impedance has been checked to be independent of the current magnitude I_x (Jougnot et al., 2010). The impedance is estimated as $Z_m = U_m/I_s = R_s U_m/U_s \approx Z_x$ for a current excited by a 5-V difference in applied voltage; we have $I_x \approx I_s = U_s/R_s = 5$ mA, where $R_s = 1$ Kohm is the resistance at the shunt resistor. The expression of the complex impedance can be written as

$$Z*(\omega) = |Z*(\omega)|e^{i\varphi(\omega)}, \tag{26}$$

where $|Z*(\omega)|$ is the impedance magnitude in ohms, and $\varphi(\omega)$ is the frequency-dependent phase angle in milliradians, obeying ohm's law as $Z(\omega) = U(\omega)I(\omega)^{-1}$. Once the impedance is obtained, we determine the geometrical factor and we determine the in-phase and quadrature conductivities of the core samples in different directions with a nominal repeatability within a standard deviation of 0.25 for in-phase and 0.2 for quadrature conductivities (see Woodruff et al., 2014). The uncertainty of the measurements was determined over three cycles per frequency. Example complex conductivity spectra are shown in Figure 7b. Because conductivity is sensitive to temperature (typically 2% change per degree Celsius), temperature was maintained at 20 ± 1°C controlled by the ambient laboratory thermostat.

EXPERIMENTAL RESULTS

Isothermal electrical and elastic data sets were jointly acquired such that the properties derived from the two data sets are directly comparable at a given stress state. The Joule dissipation effect associated with the current was too small to generate notable change in the temperature of the core sample; so, all the measurements can be considered to have been done in isothermal conditions. These data yield a direct measure of the components of the complex conductivity and undrained stiffness tensors, which both depend on the textural changes in the sample due to the mechanical deformation proportional to the known effective pressure imposed in each experiment. The confining pressure P_c (MPa) is applied externally to the jacket, and the pore pressure P_p (MPa) is controlled inside the jacket during the experiment. This allows us to control the effective pressure $P*$ (MPa) applied to the core sample.

Repeated ultrasonic and spectral-induced polarization were first acquired for the as-received drained sample under hydrostatic confining pressure P_c from 0 to 34.5 MPa for the loading and unloading sequences. The term *drained sample* is used here in its classical poroelastic meaning: The sample is water saturated, but the fluid does not resist compaction because we give it the time to flow through the pore space in response to loading. Subsequent undrained experiments were made along lines of constant pore pressure P_p from 0 to 17.25 MPa, over sequential confining pressure P_c loops up to 35.4 MPa at pressure increments of 3.45 or 6.98 MPa per stage. Undrained zero-stress measurements $P_d = 0$ MPa were made at the same confining pressure interval. Figure 8 depicts the pressure matrix of the undrained experiments. At the maximum differential pressure state of 34.47 MPa, the sample may not behave as a pure poroelastic composite. (Damage is commonly observed due to the highly heterogeneous nature and fissility in shales.) In this work, we provide an analysis along lines of constant pore pressure and differential stress, but the measurements were made only along lines of constant pore pressure.

Experiments were performed with jacketed samples under hydrostatic confinement in hydraulic oil. A nominal gradient of 140 kPa min^{-1} was used throughout the various acquisitions. The required pressure was reached when the pump flow rate fluctuated around 0.1 ml/min for that pressure. Prior to each acquisition, we condition the sample in a stress loop from 0 to 13.79 MPa (70 kPa min^{-1}), allowing for stress equilibration at the maximum pressure. Equilibration times were determined during the first few measurements through repeated ultrasonic tests. Measured waveforms were compared until the elastic response stabilized, yielding an equilibration period of 30 min per pressure stage. We collected the compressional and shear waveforms and impedance spectra at each of the pressure steps. Data were acquired at log-distributed frequencies ranging from 100 mHz to 10 Hz.

The pressure dependence of the elastic wave velocity and complex conductivity is associated to porosity changes. We observe a monotonic increase in velocity with increasing differential pressure (Figure 9) and a corresponding monotonic decrease in complex conductivity (Figures 10 and 11). The drained measurements were made prior to the undrained measurements. These data comprise the initial stress cycle to which the core was exposed (loading and unloading from 0 to 34.5 MPa). The sample was taken well

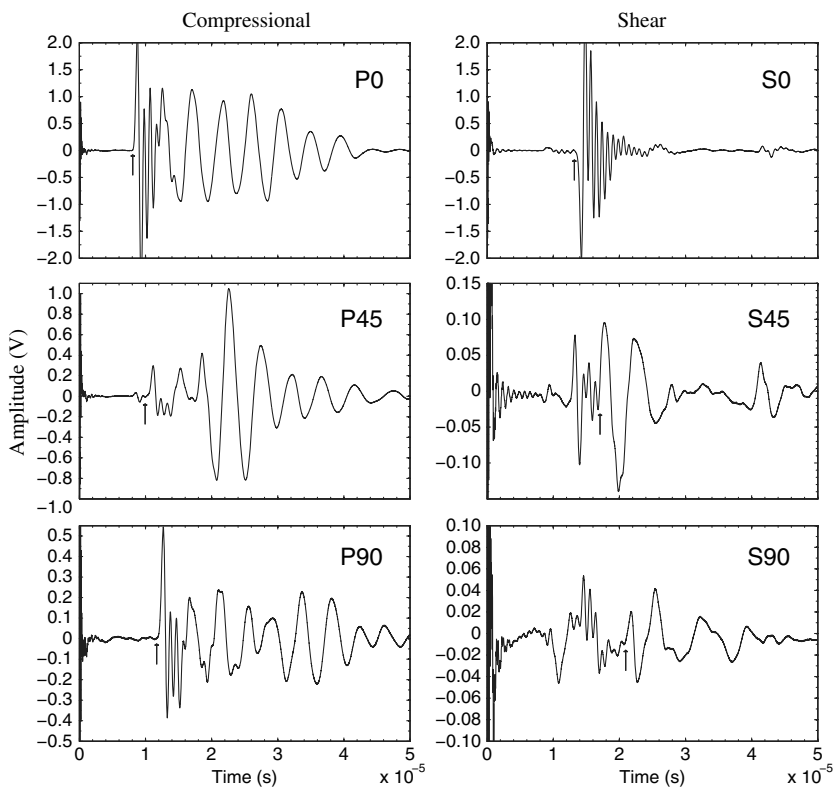

Figure 6. Examples of ultrasonic waveforms. Group velocity picks are within 2% for compressional and 4% for shear. The vertical arrows show the arrival times.

beyond the fracture closure pressure (approximately 20 MPa) to identify and characterize the poroelastic response before and after closure of these cracks.

INTERPRETATION OF LABORATORY MEASUREMENTS

Effective pressure for the ultrasonic velocity

Elastic tensor components were obtained from in the in-plane C_{11} and transverse C_{33} compressional and in-plane C_{66} and transverse C_{44} S-wave velocities using equations 5–10 (see Table 3). We analyze the tensor components along lines of constant differential stress and lines of constant pore pressure in the respective directions. These data are shown in Figures 12 and 13. We are able to delineate two stress regimes in the elastic properties, the subclosure (dark circles with solid lines) and superclosure (light circles with dashed lines) fracture closure pressure measurements corresponding to open and closed fracture networks, respectively. Even though these regimes are analogous to those described in the undrained experiments, the fracture closure pressure is now somewhere between 10 and 15 MPa, therefore significantly lower than in the drained experiments. We believe that this behavior is the result of changes in the fracture compliance between the experiments; the undrained experiments exhibit much weaker, more compliant fractures than the initial drained experiments (i.e., the sample was strained and possibly fractured by the drained experiments).

Lines of constant differential stress exhibit a change in slope with increasing confining stress in the in-plane and transverse moduli, with slopes increasing for compressional moduli (C_{11} and C_{33}) and decreasing for shear moduli (C_{66} and C_{44}) to constant gradients above fracture closure. The effective stress coefficient was estimated from these gradients for measurements at subclosure and superclosure differential pressure conditions using equation 3. Given the scatter in the data, a predominant slope was selected to represent the numerator. For measurements made at low differential stress (below fracture closure), we obtain the following effective stress coefficients for the components of the undrained stiffness tensor: $\alpha_{11} = 0.67$, $\alpha_{33} = 0.90$, $\alpha_{44} = 0.69$, and $\alpha_{66} = 0.93$ (see the definition in Appendix B). Measurements made under high differential loading (above fracture closure) yielded significantly lower effective stress coefficients: $\alpha_{11} = 0.02$, $\alpha_{33} = 0.31$, $\alpha_{44} = 0.50$, and $\alpha_{66} = 0.37$. This result shows the increased sensitivity of ultrasonic measurements to pore pressure with open fractures when compared to the same sample with closed fractures.

The stress dependence of the velocity is dependent on the increase in the density associated with the compaction of the sample under increasing hydrostatic load. Indeed, the dynamic (high-frequency) mechanical characteristics of the material are described by elastic moduli (i.e., components of the stiffness tensor) obtained directly from the compressional and shear velocities measured across the sample in different directions relative to the bedding/foliation plane (equations 18–23). The mechanical response shows some irreversible deformation. Indeed, a compacted sample will not decompress completely on the time scale of the experiments and may undergo inelastic rheological changes if subjected to sufficiently compressional high-stress states. Figure 9 shows velocity increases under hydrostatic loading with higher velocities in the unloading sequence probably associated with irreversible deformation of about 2%–5%.

We observe fracture closure in the ultrasonic data as a change in slope along the stress path occurring around 20.7 MPa. Above this stress

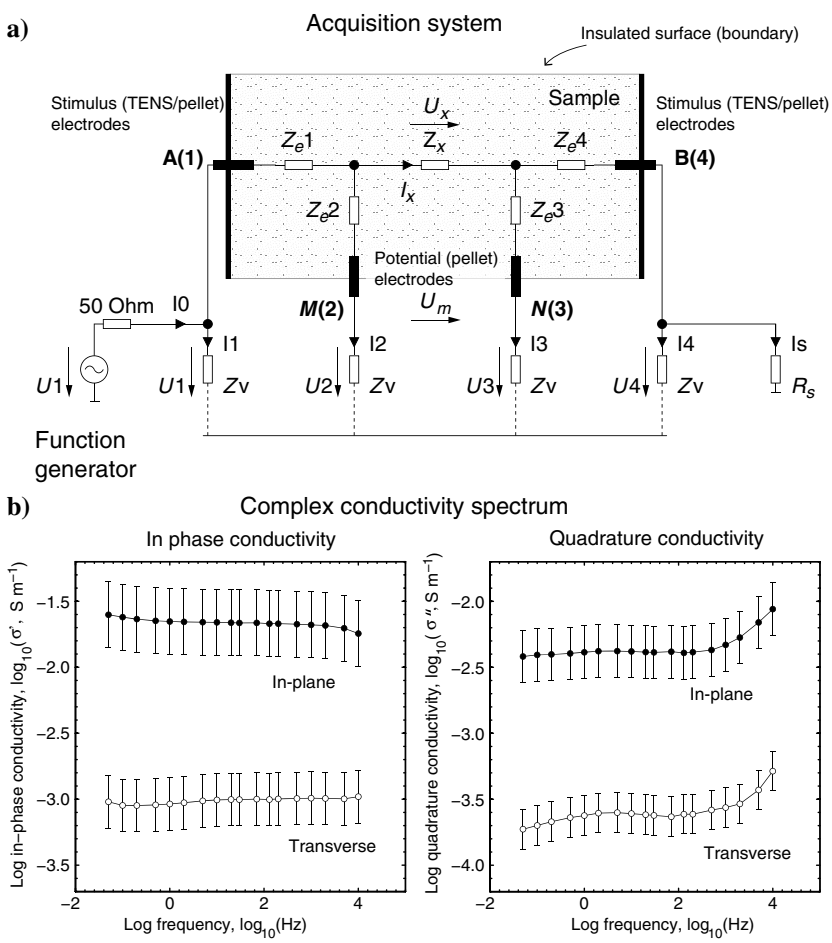

Figure 7. Impedance measurement and typical complex conductivity spectrum for the Haynesville core sample. (a) Circuit diagram of the impedance measurement. The stimulus voltage U_1 and current I_0 are modulated over at a set of predesigned frequencies ranging from 100 mHz to 10 Hz, grounded across the sample at the locations 1 and 4. The true sample impedance Z_x is calculated from the transfer current I_x in the sample, the potential drop U_x between the potential electrodes 2 and 3, and the known resistance R_s of the shunt resistor (1 kohm). Electrode contact impedances Z_e and the known input impedance Z_v (1Gohm) of the acquisition system are also depicted. Current, impedance, and voltage are measured in A, ohm, and V, respectively. (b) Typical complex conductivity spectrum (in-phase and quadrature conductivity versus frequency) for the Haynesville core sample. Nominal errors are within a standard deviation of 0.25 and 0.20 for in-phase and quadrature conductivities, respectively.

state, the rate of velocity increase with confining (differential) stress decreases in the compressional and shear measurements (Figure 9). Compressional and shear energies are sensitive to different properties and components of a porous medium. Because fluids do not support shear motion, the shear energy propagates in the solid frame, whereas the compressional energy propagates in the fluid and solid phases. Due to this phenomenon, the compressional energy is more sensitive to changes in porosity because this impacts the distribution (and density for compressible fluids) of fluids within the pore and fracture networks. We observe a more pronounced change with closure in compressional data when compared to shear data, which is attributed to the abrupt change in (saturated) fracture porosity above fracture closure pressure. Shear energy is not transmitted in the fluid phase; although fracture closure impacts the effective stress response, S-waves are not sensitive to changes in fluid distribution associated with closure. However, shear energy has higher sensitivity above closure associated with the mechanical coupling of the fracture planes (microscopic misalignment of the roughness of the fracture surfaces).

We can also make observations of the relative sensitivity of the directional measurements to fracture closure to draw inferences about the mechanical response of the sample. The sample is least sensitive to open fractures (low differential stress) for in-plane P-waves; the change in the corresponding anisotropic effective stress component is most pronounced in this direction, evidencing fracture closure nearly eliminates the pore pressure effect (Figure 10). The sample is most sensitive to S-waves polarized in the isotropic (fracture, bedding, foliation) plane (Figure 11). This behavior indicates that macroscopic fractures slow the propagation of shear energy when the fracture surfaces are decoupled in the direction of in-plane shear motion. Similarly, the transverse P-wave is also sensitive to fractures at low differential pressures when the fracture surfaces are decoupled in the direction of transverse particle motion. S-waves polarized at 90° to the isotropic plane exhibit the least sensitivity to fracture closure because this wave is polarized transverse to the fracture sets.

Effective pressure for the complex conductivity

Figures 14 and 15 show the components (in-plane and transverse) of the complex conductivity tensor as a function of the equilibrium pressure and confining pressure, respectively. We first analyze the effective stress response of the complex electrical conductivity as the change in conductivity in the in-plane and transverse directions for equilibrium measurements ($P_d = 0$). We find the poroelastic effect associated with the electrical response to be anisotropic, exhibiting a normalized increase in complex conductivity of $\overline{\Delta\sigma}* = 2.64 + 1.99i$ for the in-plane and $\overline{\Delta\sigma}* = 0.89 + 0.91i$ for the transverse conductivities, respectively. This behavior indicates the electrical response is most sensitive to pore pressure in the foliation plane (Figure 14). Several spectral-induced polarization data sets were considered to be unreliable due to noise level (determined at each frequency on three cycles). As a result, we did not obtain a complete matrix of pore pressure and differential pressure measurements, and the analysis is performed as a function of differential pressure, irrespective of the loading-unloading sequence. Anisotropic effective stress coefficients were estimated from the gradients of electrical textural tensor components F_{ij} and T_{ij} only along lines of zero differential pressure and zero pore pressure. We obtained in-plane and transverse poroelastic effective stress coefficients of $\alpha_1^F = 0.95$ (in plane) and $\alpha_3^F = 0.84$ (transverse) for the formation factor tensor and $\alpha_1^T = 0.98$ (in plane) and $\alpha_3^T = 0.51$ (transverse) for the tortuosity tensor

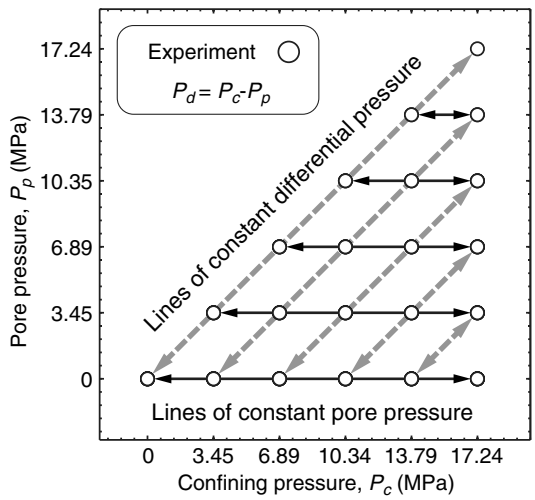

Figure 8. Sketch of the pressure matrix used for the ultrasonic and spectral-induced polarization experiments in the pore fluid pressure/confining pressure space. Drained experiments correspond to measurements along the line $P_p = 0$. Undrained experiments comprise all of the measurements shown; measurements are made in a sequence obeying the condition $P_p \leq P_c$ to ensure that the sample is not subjected to negative differential stress $P_d < 0$ that may fracture the sample depending on its tensile strength. Data are first acquired along lines of constant pore pressure in increments of 3.45 MPa (solid arrows); ultimately, the zero differential stress loop $P_d = 0$ is acquired (dashed arrow). Additional experiments along (diagonal) lines of constant differential stress may also be of interest to fully describe the effective stress dependence of the sample.

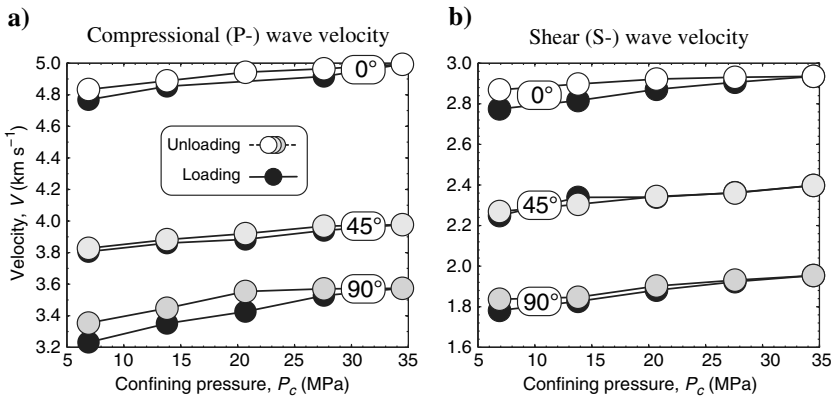

Figure 9. Drained ultrasonic measurements in the in-plane (0°), oblique (45°), and transverse (90°) directions. (a) Compressional (P-) wave velocity and (b) shear (S-) wave velocity. We observe monotonic increases in the P- and S-velocity with increased differential pressure. Higher velocities are consistent with irreversible deformation in the unloading stress stages.

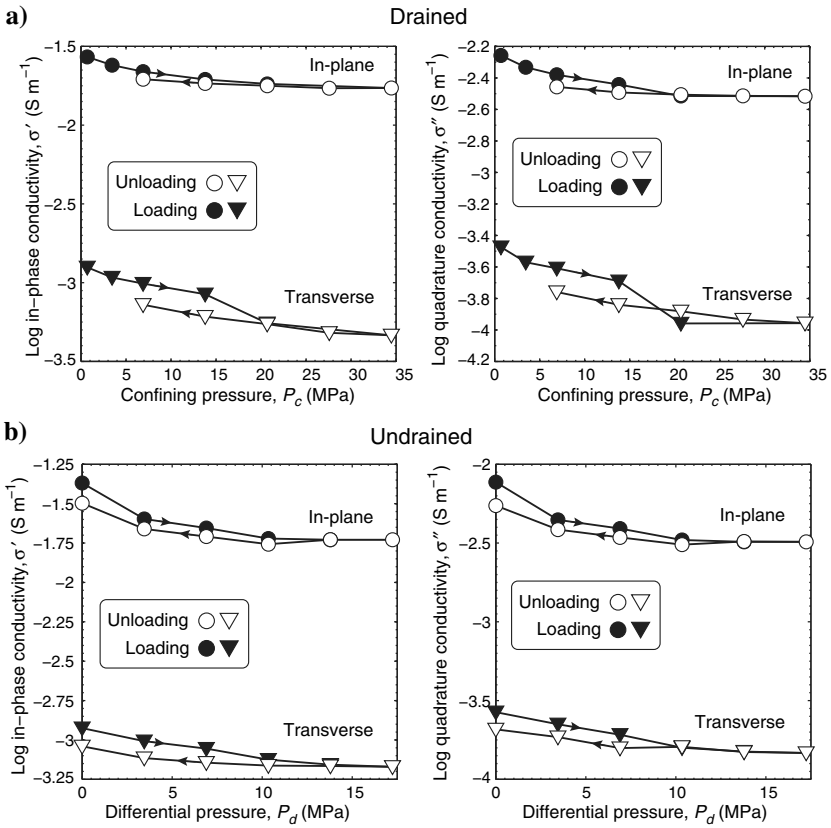

Figure 10. Complex electrical conductivity under hydrostatic loading (a) drained experiment and (b) undrained experiment. The in-phase and quadrature conductivities decrease with increased load. This behavior is due to infinitesimal changes in the textural properties, such as the porosity, with the compaction of the sample. Conductivities represent relative magnitudes calculated from the azimuthal complex impedances with a geometric factor $k = 0.323$ (dimensionless); the tensor components can be inverted from these data. The full cycle in the differential pressure shows the irreversible deformation generated in the core sample.

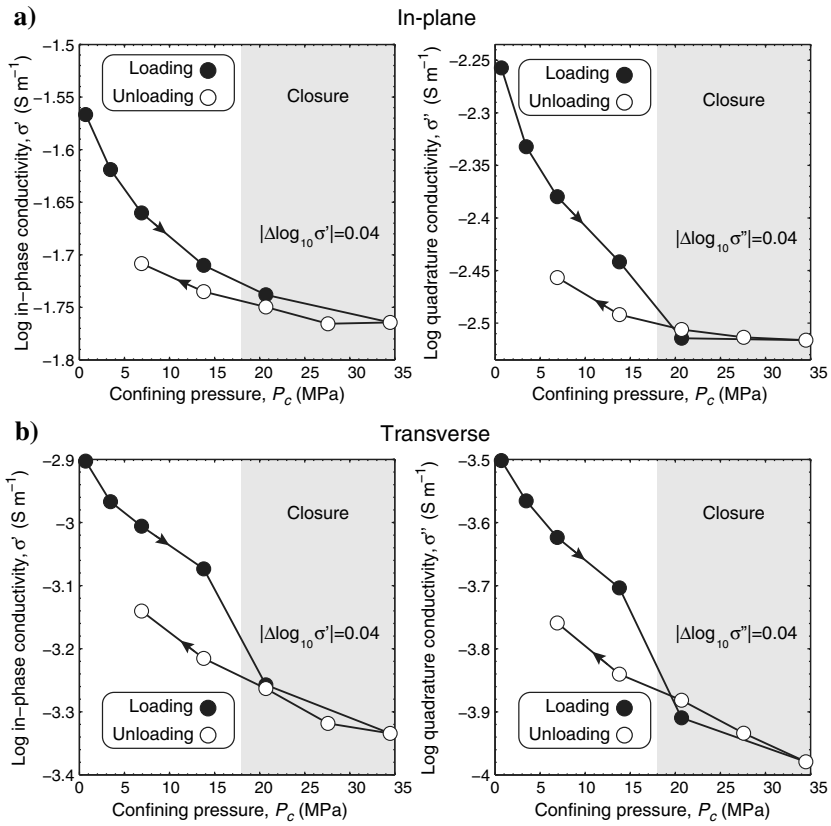

Figure 11. Drained measurements. Complex electrical conductivity decreases with increased load due to changes in the porosity (fracture closure and compaction; drained experiment). Closure is observed as a first-order reduction in conductivity at 20.68 MPa. (Differential stress exceeds the fracture closure pressure in the shaded regions.) (a) Textural fabric gives rise to second-order changes in the in-plane slope above closure; the magnitude change in the quadrature component is one quarter the in-phase component ($|\Delta\log_{10}\sigma'| = 0.04$; $|\Delta\log_{10}\sigma''| = 0.01$), indicating that the changes in tortuosity are small in correspondence with changes in surface conductivity. (b) Changes in (b) transverse in-phase and quadrature slopes are comparable ($|\Delta\log_{10}\sigma'| = 0.04$ and $|\Delta\log_{10}\sigma''| = 0.04$), indicating that the tortuosity normal to the bedding plane correlates with fracture closure and mechanical compaction. The shaded area is intended to highlight the high differential stress measurements that indicate fracture closure. The limits of this region were not obtained quantitatively.

(see the definitions in Appendix B), indicating that the stress dependence for the textural tensors is strongest in the direction transverse to the foliation plane (Figure 16).

We know that the in-phase conductivity tensor depends on the series combination of the conduction current in the pore water and the surface conduction in the Stern and diffuse layers, indicat-

Table 3. Components of the mechanical stiffness tensor C_{ij} and electrical formation factor tensor F_{ij}, and tortuosity tensor T_{ij} from the undrained experiments along the initial loading path, the $Pp = 0$ line. Fracture closure values are provided at 10.34 MPa confining pressure, bounded by the values above and below closure at 6.89 and 13.79 MPa, respectively. The in-plane and traverse translational components C_{12} and C_{13} are determined from equation 15 from Hornby (1998). Note that our results are consistent with those from Sone and Zoback (2013) for an axial pressure of 10 MPa. For their sample H-1, they obtain $C_{11} = 54$ MPa, $C_{33} = 30$ MPa, $C_{66} = 20$ MPa, and $C_{44} = 11$ MPa.

Confining pressure Pc	6.89 MPa	10.34 MPa	13.79 MPa
Stiffness tensor			
C_{11} in-plane compressional) (M)	52.38 GPa	53.54 GPa	54.21 GPa
C_{33} (transverse compressional)	24.29 GPa	26.07 GPa	26.52 GPa
C_{66} (in-plane shear)	18.87 GPa	19.03 GPa	19.12 GPa
C_{44} (transverse shear)	15.31 GPa	15.87 GPa	16.30 GPa
C_{12} (in-plane translational)	14.65 GPa	15.48 GPa	15.97 GPa
C_{13} (transverse translational)	11.34 GPa	12.66 GPa	12.89 GPa
Textural tensors			
F_1 (in-plane formation factor)	251	261	255
F_3 (transverse formation factor)	3698	3819	5470
τ_1 (in-plane tortuosity)	15	18	20
τ_3 (transverse tortuosity)	185	180	227

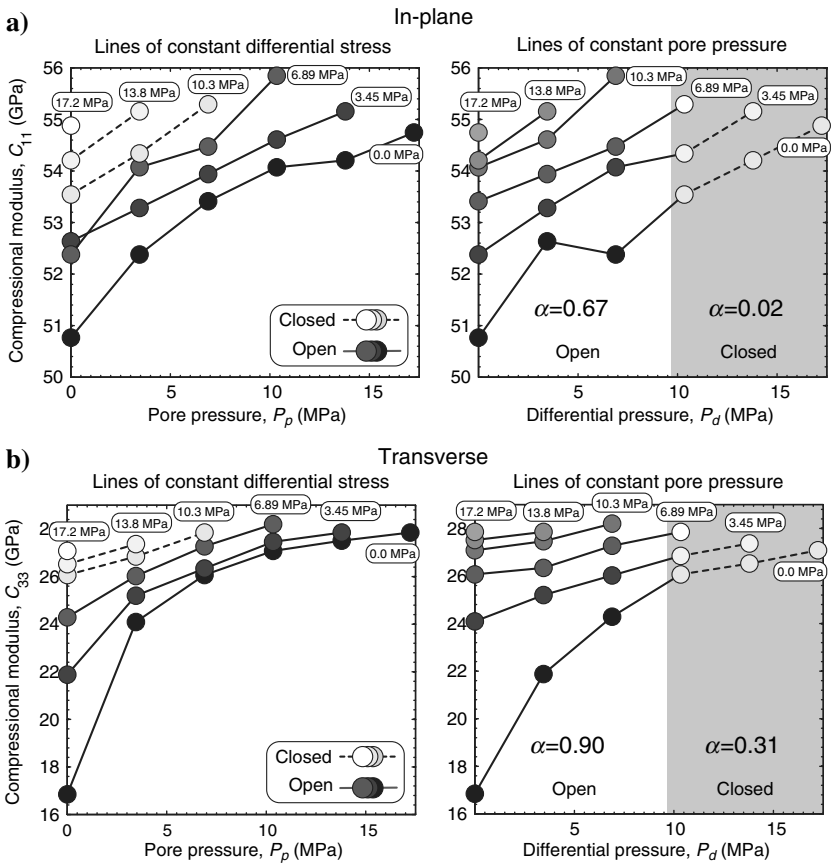

Figure 12. Effective stress behavior for the stiffness tensor components. (a) In-plane C_{11} and (b) transverse C_{33} compressional moduli along lines of constant differential stress and constant pore pressure. The effective stress coefficient is computed as the ratio of the gradients of differential stress lines to pore pressure lines. Values are obtained below (dark circles with solid lines) and above (light circles with stippled lines) fracture closure. These results indicate a strong dependence of the effective stress response to the fractures in the sample. The shaded area is intended to highlight the high differential stress measurements that indicate fracture closure. The limits of this region were not obtained quantitatively.

ing correlation with the conductivity magnitude through the porosity (including the directional dependence of the formation factor and tortuosity tensors), whereas the quadrature conductivity tensor also depends on the textural changes through the tortuosity tensor (refer to the respective in-phase and quadrature forms in equations 13 and 14). Therefore, we expect the first-order stress dependence of the complex conductivity to be tied to the direction of deformation. For a hydrostatic load, this is expected to occur in the direction normal to the bedding plane (transverse direction); i.e., the change in electrical conductivity is greater in the transverse direction, but there is greater sensitivity to the effective pressure change in the plane of isotropy (in plane).

We observe a decrease in the complex conductivity of a quarter order of magnitude in the undrained in-plane measurements, and a decrease in nearly half an order of magnitude in the transverse direction, with the sample stabilizing at 20.7 MPa in the drained experiments (see Figure 10). The stabilization can be attributed to the closing of the fracture porosity observed in the sample. The in-plane measurements exhibit a conductivity change over 1.5 orders greater (approximately a factor 30) than the transverse to bedding/foliation plane.

We expect the second-order sensitivity to arise because of differences in the in-phase and quadrature conductivities. The in-phase component should be more sensitive to stress (i.e.,

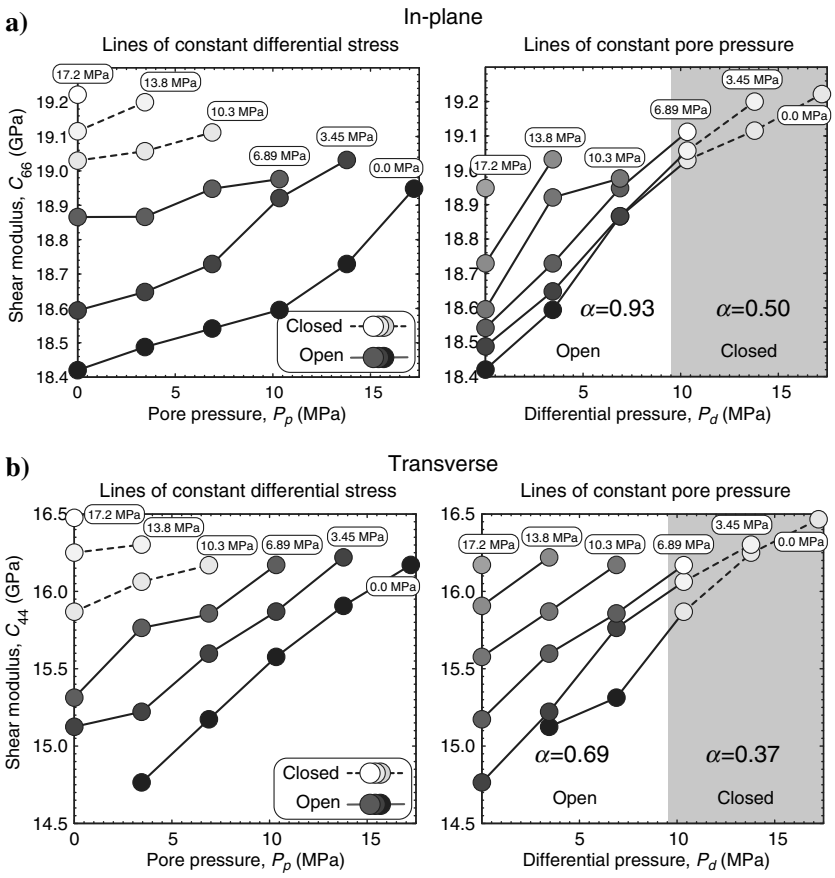

Figure 13. Effective stress behavior for the stiffness tensor components. (a) In-plane component C_{66}. (b) Transverse C_{44} shear moduli along lines of constant differential stress and constant pore pressure. The effective stress coefficient is computed as the ratio of the gradients of differential stress lines to pore pressure lines. Values are obtained below (dark circles with solid lines) and above (light circles with stippled lines) the fracture closure, which indicates a strong dependence of the effective stress response to the fractures in the sample. The shaded area is intended to highlight the high differential stress measurements that indicate fracture closure. The limits of this region were not obtained quantitatively.

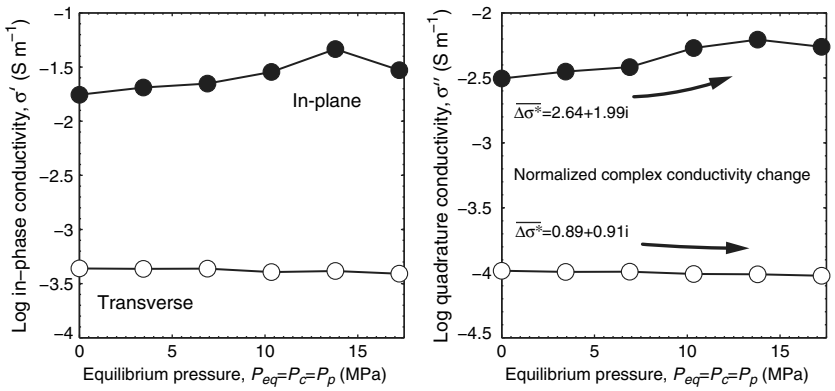

Figure 14. Complex electrical conductivity change in the in-plane and transverse directions for equilibrium measurements ($P_d = 0$). The electric poroelastic effect is anisotropic. Normalized increases in in-plane and transverse complex conductivities are calculated as the ratio of the minimum and maximum in-phase and quadrature conductivities. We obtain $\overline{\Delta\sigma*} = 2.64 + 1.99i$ in the in-plane direction and $\overline{\Delta\sigma*} = 0.89 + 0.91i$ in the transverse direction. This indicates that the electrical response has the highest sensitivity to pore pressure in the foliation plane, probably because the cracks are oriented in this plane.

mechanical compaction) than the quadrature component due to the in-phase sensitivity to changes in conduction in fractures and macroporosity, and this sensitivity should increase with salinity as the conduction current increases. Changes in the textural fabric above closure (20.7 MPa) give rise to second-order changes in the slope of the in-plane measurements associated with reduced tortuosity (e.g., the infinitesimal realignment of clay minerals; Figure 11). The magnitude change in the quadrature component is one-quarter that of the in-phase component ($|\Delta \log_{10} \sigma'| = 0.03$ and $|\Delta \log_{10} \sigma''| = 0.01$), indicating that changes in tortuosity are small in correspondence with the change in surface conductivity. Changes in transverse in-phase and quadrature slopes are comparable ($|\Delta \log_{10} \sigma'| = 0.04$ and $|\Delta \log_{10} \sigma''| = 0.04$), indicating that the tortuosity normal to the bedding plane correlates with fracture closure and compaction.

Figure 17 compares the stress dependence for the drained and undrained acquisitions. Here, we once more observe evidence of an irreversible component of strain in both acquisitions. Indeed, the undrained experiments appear to follow the measurements along the unloading sequence of the drained measurements, indicating that the sample did not return to its initial condition. The loading path of the complex conductivity follows the drained acquisition and rebounds at a lower complex conductivity in the unloading sequence in in-plane and transverse directions. This response is further evidence of damage due to compaction. In-phase and quadrature conductivities exhibit a reduced rate of change as the fractures reopen with decreasing differential stress.

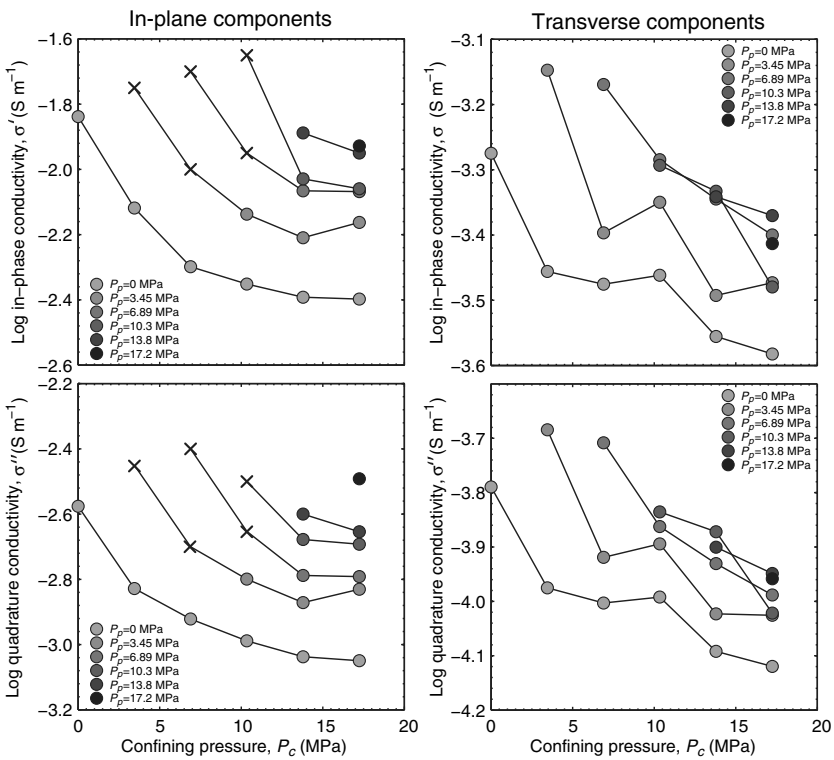

Figure 15. Complex electrical conductivity as a function of the confining pressure. (a) In-plane components of the in-phase and quadrature conductivities. (b) Transverse components of the in-phase and quadrature conductivities. The crosses represent extrapolated data and are provided estimates as a visual aid.

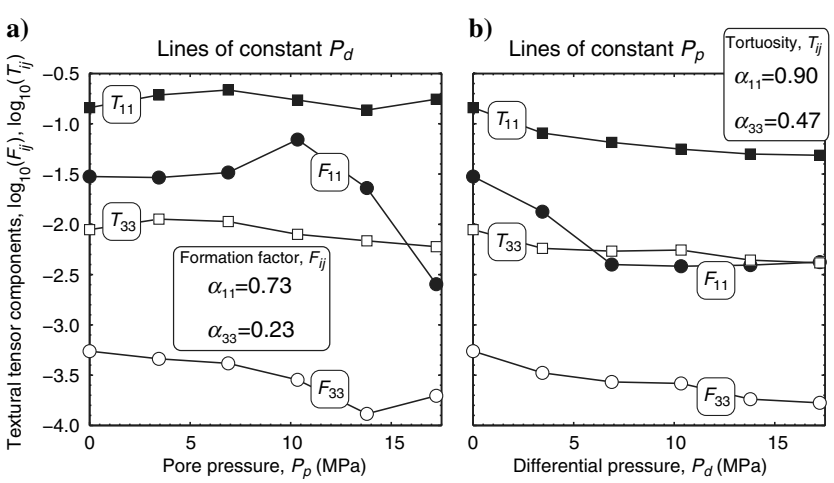

Figure 16. Complex electrical conductivity effective stress coefficients for the formation factor and tortuosity tensors. The relative magnitude of the effective stress components indicates higher sensitivity in the foliation/bedding plane. Plots identify lines of constant differential ($P_d = 0$) pressure and constant pore fluid pressure ($P_p = 0$).

Evolution of the anisotropy factor

In Table 3, we can see the values of the formation factor and tortuosities for the in-plane and transverse directions. The complex conductivity anisotropy factor was computed as the ratio of the in-plane and transverse in-phase and quadrature conductivities, respectively (Figure 18). From these data, it seems that the realignment of the platy clay minerals is affected by the increased mechanical load, and therefore, complex conductivity anisotropy increases with differential pressure (Figure 18). At low differential pressure, the closure of the cracks is also captured by the change in the anisotropy ratio with differential pressure along the respective loading and unloading paths. The anisotropy of the electrical response remains higher with each successive loading-unloading stress loop, indicating that the sample does not fully return to the initial condition. Above crack closure, the material behaves elastically.

EFFECTIVE STRESS COEFFICIENTS

Figure 19 shows four of the components of the stiffness tensor as the function of the effective pressure $P* = P_c - \alpha_i^{\chi} P_p$. Figure 19a–19d shows the four components as a function of the effective stress, $P*$ assuming that the effective pressure coefficient is independent of the differential pressure. The different curves do not collapse into a single master curve indicating that the effective

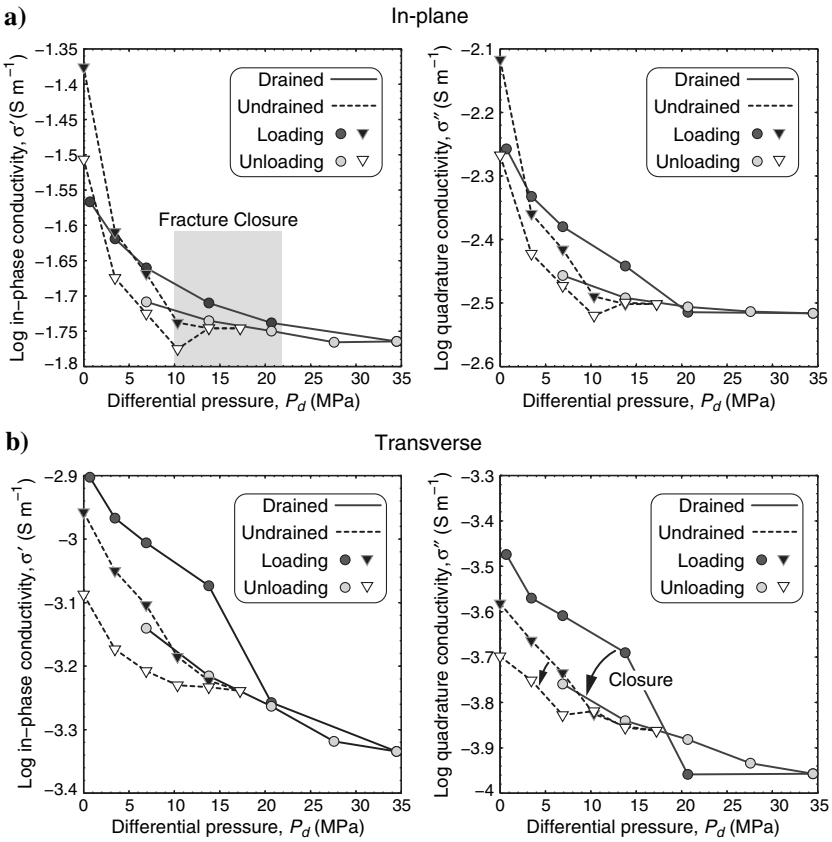

Figure 17. Stress-induced strain curves in the complex electrical conductivity for drained (circles) and undrained (triangles) experiments in the (a) in-plane and (b) transverse directions. Fracture closure occurs at 20 MPa (drained) and between 10 and 15 MPa (undrained) due to changes in the fracture compliance between experiments. The change in slope along the unloading and unloading stress paths indicates that the sample undergoes irreversible changes with successive stress loops (note undrained loading data follow the drained unloading path).

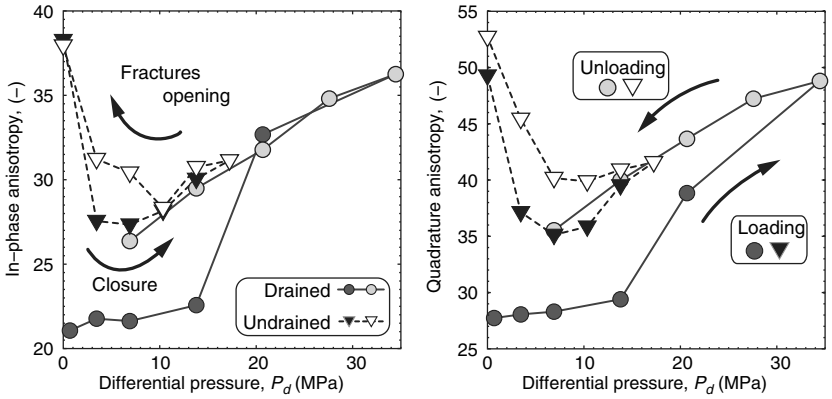

Figure 18. Complex electrical conductivity anisotropy factor for drained (circles) and undrained (triangles) acquisitions. Fracture effects are captured by the change in the anisotropy ratio with differential pressure along the respective loading and unloading paths. Anisotropy remains higher with successive loading (dark) and unloading (light) loops, indicating that the sample does not fully decompress or return to the initial condition. The material behaves elastically above the fracture closure, indicating that compaction of the sample at these confining pressures is elastic and damage is largely associated with the fractures. The anisotropy factor is calculated as the ratio of the in-plane and transverse in-phase and quadrature conductivities; i.e., $\lambda' = \sigma_0'/\sigma_{90}'$ and $\lambda' = \sigma_0''/\sigma_{90}''$ (both dimensionless), respectively.

stress coefficients are stress dependent. Figure 19e–19h accounts for the stress dependence with the differential pressure, collapsing the data into a master curve. The effective stress laws for transverse and in-plane electrical conductivity tensor components are shown in Figure 20. We see a general decrease of the components of the complex conductivity tensor with effective stress and

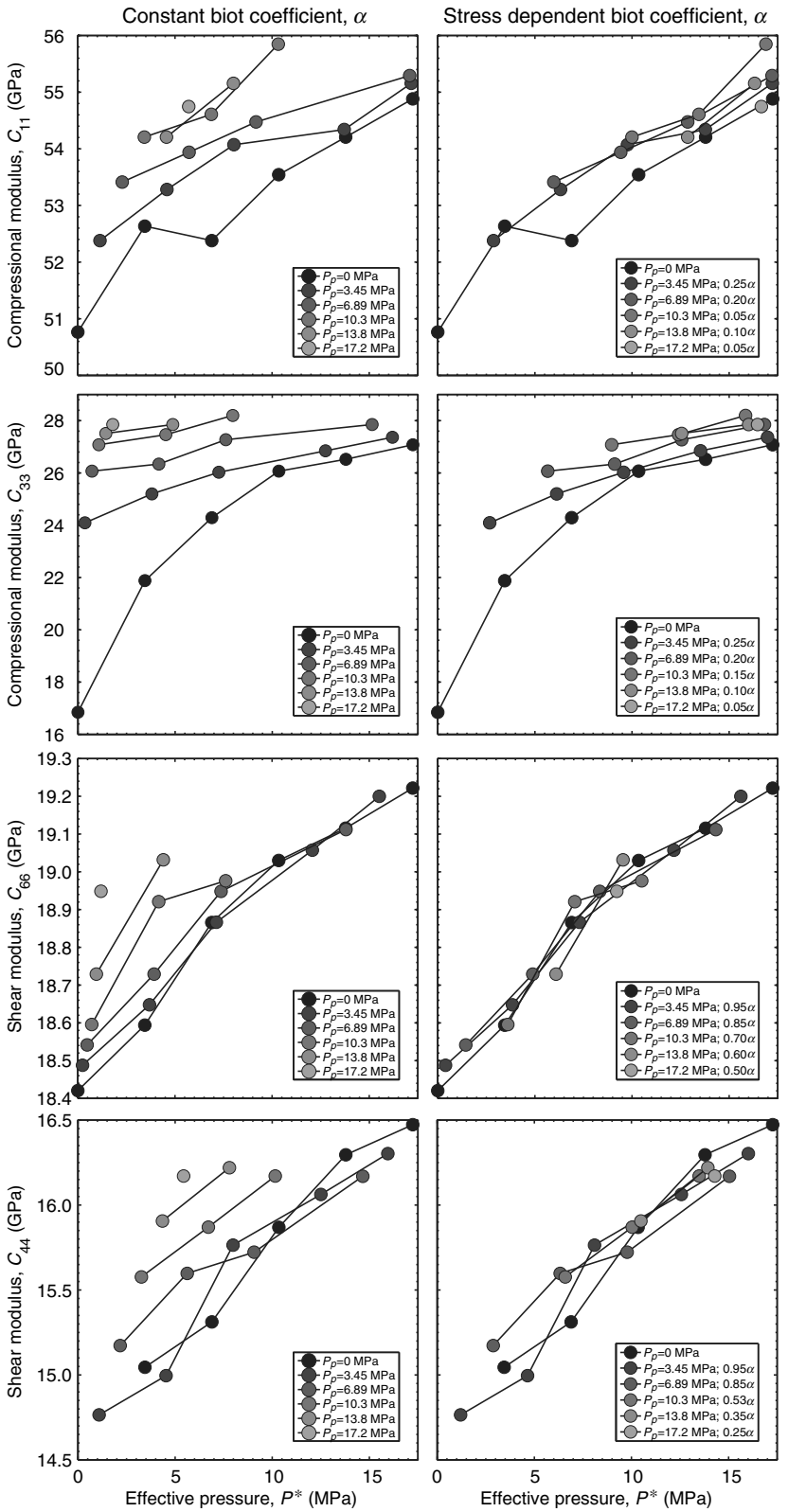

Figure 19. Effective stress law for the components of the stiffness tensor $\mathbf{C}^u$ using $\alpha_{11} = 0.67$, $\alpha_{33} = 0.90$, $\alpha_{44} = 0.69$, and $\alpha_{66} = 0.93$ below fracture closure and $\alpha_{11} = 0.02$, $\alpha_{33} = 0.31$, $\alpha_{44} = 0.50$, and $\alpha_{66} = 0.37$ above. (a-d) The effective stress coefficient is independent of the differential pressure, and (e-h) the effective stress coefficient is dependent on the differential pressure.

an effective stress coefficient that is scaled dependent upon the stress state.

Because we did not directly measure deformation in these experiments, we obtain a measure of porosity compaction from the ratios of the textural tensor components $F_{ij}T_{ij}^{-1}$. The porosity mean and standard deviation versus effective stress indicate porosity reduction on the order of 0.03 with increased effective stress as shown in Figure 21. Note that the starting porosity is consistent with the mass density used in this work (2450 kg m^{-3}). Low-porosity shales such as the one used in our study show usually <0.5% absolute porosity reduction (D. Dewhurst, personal communication, 2015). Therefore, in future experiments, it will be interesting to measure directly the deformation of the core sample and the amount of fluids released during compaction to have a complete description of the components of the drained stiffness tensor and therefore to obtain a complete characterization of the poroelastic parameters of the material.

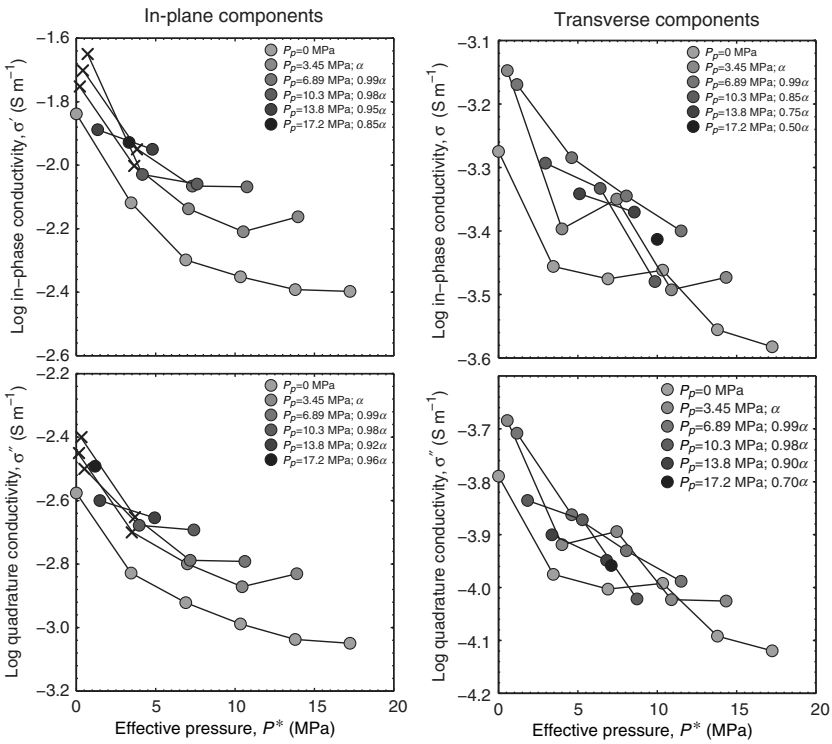

Figure 20. Effective stress law for the in-plane and transverse components of the complex conductivity tensor. The crosses correspond to extrapolated data. The values of the pressure dependence effective stress coefficient are provided on the graphs using the effective stress coefficients obtained for the tortuosity $\alpha_{11} = 0.98$ and $\alpha_{33} = 0.51$

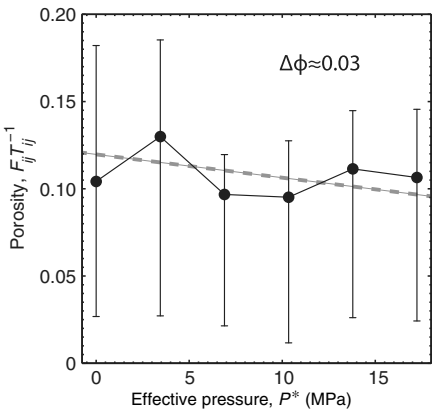

Figure 21. Effective stress law for the porosity as determined from the relationship between the components of the formation factor tensor and those of the tortuosity tensor.

CONCLUSIONS

We have described the effective stress coefficients for the components of the stiffness and complex conductivity tensors of a transverse isotropic core sample taken from the Haynesville gas shale formation. The following conclusions have been reached:

1) We have found that surface conductivity is a very important contribution to the overall electrical conductivity of the Haynesville. The anisotropy ratio for the in-phase and quadrature components is between 20 to 50, and it depends on the differential stress and shows an increase associated with the closure of the cracks. The anisotropy of the seismic properties corresponds to a factor of 2.
2) Two pressure regimes were identified as delimited by the crack closure pressure (around 10 to 20 MPa in differential pressure). We have determined the effective stress coefficients for the components of the undrained stiffness tensor and the components of the formation factor and tortuosity tensors. The effective stress coefficients are much higher in the low-effective-pressure regime (cracks open) than in the high-effective- pressure regime (cracks closed).

Even though the results presented in this work should not be generalized to characterize the Haynesville gas shale (because we investigated only one core sample with cracks), they can be broadly applied to better understand the poroelastic behavior of tight, clay-rich shales, and mudstones with microcracks, providing a basis to describe the multiphysical connections between geophysical measurements and the mechanical deformation of unconventional reservoir rocks.

ACKNOWLEDGMENTS

This paper is dedicated to M. Batzle for his huge contributions to the field of petrophysics. This work was funded by the OCLASSH consortium and the University of Texas at Austin's Research Consortium on Formation Evaluation, jointly sponsored by Anadarko, Apache, Aramco, Baker-Hughes, BG, BHP Billiton, BP, Chevron, China Oilfield Services, LTD., ConocoPhillips, ENI, ExxonMobil, Halliburton, Hess, Maersk, Marathon Oil Corporation, Mexican Institute for Petroleum, Nexen, ONGC, Petrobras, Repsol, RWE, Schlumberger, Shell, Statoil, Total, and Weatherford. We also thank the support from the Colorado School of Mines Unconventional

Natural Gas and Oil Institute (UNGI) CIMMM Consortium sponsors for the support of this research. We thank E. Zimmerman at Forschungszentrum Jülich for developing and building the low-frequency impedance spectrometers used in this work, R. Sharma for his help in designing the sample holder, and S. Rivera, and L. Ou for their help in all aspects of the experimental program. We thank two anonymous referees and D. Dewhurst for their constructive reviews.

APPENDIX A

EFFECTIVE STRESS COEFFICIENT

In this appendix, we show how the effective stress coefficient can be defined for any transport property $\chi(P_d, P_p)$ where $P_d = P_c - P_p$ denotes the differential pressure (see Todd and Simmons [1972] for the P-wave velocity in the isotropic case). We start with the total differential:

$$d\chi = \left(\frac{\partial \chi}{\partial P_p}\right)_{P_d} dP_p + \left(\frac{\partial \chi}{\partial P_d}\right)_{P_p} dP_d. \tag{A-1}$$

Equation A-1 can be written as

$$d\chi = \left[\left(\frac{\partial \chi}{\partial P_p}\right)_{P_d} - \left(\frac{\partial \chi}{\partial P_d}\right)_{P_p}\right] dP_p + \left(\frac{\partial \chi}{\partial P_d}\right)_{P_p} dP_c \tag{A-2}$$

and

$$d\chi = \left(\frac{\partial \chi}{\partial P_d}\right)_{P_p} \left\{\left[\frac{\left(\frac{\partial \chi}{\partial P_p}\right)_{P_d}}{\left(\frac{\partial \chi}{\partial P_d}\right)_{P_p}} - 1\right] dP_p + dP_c\right\}. \tag{A-3}$$

Equation A-3 can be written as

$$d\chi = \left(\frac{\partial \chi}{\partial P_d}\right)_{P_p} dP*, \tag{A-4}$$

where the effective pressure $P*$ for the property χ is defined as $dP* = dP_c - \alpha_\chi dP_p$ (effective pressure law), and the effective stress coefficient as

$$\alpha_\chi = 1 - \frac{\left.\frac{\partial \chi}{\partial P_p}\right|_{P_d}}{\left.\frac{\partial \chi}{\partial P_d}\right|_{P_p}}. \tag{A-5}$$

We will use this formulation in this paper. In the close vicinity of a stress state, we can consider that the effective stress coefficient is constant (the isolines in the state of stress (P_p, P_d) can be approximated by parallel straight lines) and the effective pressure becomes $P* = P_c - \alpha_\chi P_p$. Note, however, that another formulation is possible by using $\chi(P_c, P_p)$. In this case, we can write the total differential as

$$d\chi = \left(\frac{\partial \chi}{\partial P_p}\right)_{P_c} dP_p + \left(\frac{\partial \chi}{\partial P_c}\right)_{P_p} dP_c \tag{A-6}$$

and

$$d\chi = \left(\frac{\partial \chi}{\partial P_c}\right)_{P_p} \left[dP_c + \frac{\left(\frac{\partial \chi}{\partial P_p}\right)_{P_c}}{\left(\frac{\partial \chi}{\partial P_c}\right)_{P_p}} dP_p\right]. \tag{A-7}$$

Therefore, we can write the effective pressure law as

$$d\chi = \left(\frac{\partial \chi}{\partial P_c}\right)_{P_p} dP*, \tag{A-8}$$

where the effective pressure $P*$ for the property χ is defined as $dP* = dP_c - \alpha_\chi dP_p$ (effective pressure law), and the effective stress coefficient as

$$\alpha_\chi = -\frac{\left(\frac{\partial \chi}{\partial P_p}\right)_{P_c}}{\left(\frac{\partial \chi}{\partial P_c}\right)_{P_p}}. \tag{A-9}$$

In both cases, when the effective stress coefficient is close to one, we recover Terzaghi's definition of the effective stress (e.g., De Boer and Ehlers, 1990) with the confining and the pore fluid pressures playing opposite role on the variation of the property χ.

APPENDIX B

EFFECTIVE STRESS COEFFICIENTS FOR THE STIFFNESS TENSOR

Using the results of Appendix A, we can write the effective stress law in incremental form for the components of the undrained stiffness tensor:

$$dC_{11} = \left(\frac{\partial C_{11}}{\partial P_d}\right)_{P_p} (P_c - \alpha_{11} P_p), \tag{B-1}$$

$$dC_{33} = \left(\frac{\partial C_{33}}{\partial P_d}\right)_{P_p} (P_c - \alpha_{33} P_p), \tag{B-2}$$

$$dC_{44} = \left(\frac{\partial C_{44}}{\partial P_d}\right)_{P_p} (P_c - \alpha_{44} P_p), \tag{B-3}$$

$$dC_{66} = \left(\frac{\partial C_{66}}{\partial P_d}\right)_{P_p} (P_c - \alpha_{66} P_p), \tag{B-4}$$

$$dC_{12} = \left(\frac{\partial C_{12}}{\partial P_d}\right)_{P_p} (P_c - \alpha_{12} P_p), \tag{B-5}$$

and

$$dC_{13} = \left(\frac{\partial C_{13}}{\partial P_d}\right)_{P_p} (P_c - \alpha_{13} P_p), \tag{B-6}$$

and where the different effective stress coefficients are defined by Equation A-5 of Appendix A. Similar equations can be developed for the components of the conductivity formation tensor:

$$dF_1 = \left(\frac{\partial F_1}{\partial P_d}\right)_{P_p} (P_c - \alpha_1^F P_p), \tag{B-7}$$

$$dF_3 = \left(\frac{\partial F_3}{\partial P_d}\right)_{P_p} (P_c - \alpha_3^F P_p), \tag{B-8}$$

and for the components of the tortuosity tensor,

$$d\tau_1 = \left(\frac{\partial \tau_1}{\partial P_d}\right)_{P_p} (P_c - \alpha_1^T P_p) \tag{B-9}$$

and

$$d\tau_3 = \left(\frac{\partial \tau_3}{\partial P_d}\right)_{P_p} (P_c - \alpha_3^T P_p). \tag{B-10}$$

In these equations, we have two effective stress coefficients for the formation factor and two others for the tortuosity tensor. All of the effective stress coefficients described in this appendix are not necessarily equal or related to the component of the tensor **A** described in the main text, that is, to the two effective stress coefficients entering the effective pressure relationship.

REFERENCES

Backus, G. E., 1962, Long-wave elastic anisotropy produced by horizontal layering: Journal of Geophysical Research, **67**, 4427–4440, doi: 10.1029/JZ067i011p04427.

Bernabé, Y., 1987, The effective pressure law for permeability during pore pressure and confining pressure cycling of several crystalline rocks: Journal of Geophysical Research, **92**, 649–657, doi: 10.1029/JB092iB01p00649.

Biot, M. A., 1955, Theory of elasticity and consolidation for a porous anisotropic solid: Journal of Applied Physics, **26**, 182–185, doi: 10.1063/1.1721956.

Biot, M. A., 1956, Theory of propagation of elastic waves in a fluid saturated porous solid — Part I: Low frequency range: Journal of the Acoustic Society, **28**, 168–178.

Biot, M. A., 1962, Mechanics of deformation and acoustic propagation in porous media: Journal of Applied Physics, **33**, 1482–1498, doi: 10.1063/1.1728759.

Biot, M. A., and D. G. Willis, 1957, The elastic coefficients of the theory of consolidation: Journal of Applied Mechanics, **24**, 594–601.

Breeden, D., C. Dougan, D. Shank, and S. Summers, 2011, Haynesville performance review: Unique clay-free water-based polymer drilling fluid system for application-specific unconventional shale production intervals: Presented at 2011 AADE National Technical Conference.

Carroll, M. M., 1979, An effective stress law for anisotropic elastic deformation: Journal of Geophysical Research, **84**, 7510–7512, doi: 10.1029/JB084iB13p07510.

Chalmers, G. R., M. Bustin, and I. M. Power, 2012, Characterization of gas shale pore systems by porosimetry, pycnometry, surface area, and field emission scanning electron microscopy/transmission electron microscopy image analyses: Examples from the Barnette, Woodford, Haynesville, Marcellus and Doig units: AAPG Bulletin, **96**, 1099–1119.

Cheng, A. H.-D., 1997, Material coefficients of anisotropic poroelasticity: International Journal of Rock Mechanics and Mining Science, **34**, 199–205.

Coyner, K. B., 1984, Effects of stress, pore pressure, and pore fluids on bulk strain, velocity, and permeability in rocks: Ph.D. thesis, Massachusetts Institute of Technology.

de Boer, R., and W. Ehlers, 1990, The development of the concept of effective stress: Acta Mechanica, **83**, 77–92, doi: 10.1007/BF01174734.

Dewhurst, D. N., and A. F. Siggins, 2006, Impact of fabric, microcracks and stress field on shale anisotropy: Geophysical Journal International, **165**, 135–148, doi: 10.1111/j.1365-246X.2006.02834.x.

Elgmati, M., H. Zhang, B. Bai, R. Flori, and Q. Qu, 2011, Submicron-pore characterization of shale gas plays, Presented at North America Unconventional Gas Conference and Exhibition, 144050.

Frenkel, J., 1944, On the theory of seismic and seismoelectric phenomena in a moist soil: Journal Physics (Soviet), **8**, 230–241.

Ghabezloo, S., J. Sulem, S. Guédon, and F. Martineau, 2008, Effective stress law for the permeability of a limestone: International Journal of Rock Mechanics and Mining Science, **46**, 297–306, doi: 10.1016/j.ijrmms.2008.05.006.

Giot, R., A. Giraud, T. Guillon, and C. Auvray, 2012, Three-dimensional poromechanical back analysis of the pulse test for transverse isotropy: Acta Geotechnica, **7**, 151–165, doi: 10.1007/s11440-012-0158-7.

Han, T., A. I. Best, J. Sothcott, and L. M. MacGregor, 2011a, Joint elastic-electrical properties of reservoir sandstones and their relationships with petrophysical parameters: Geophysical Prospecting, **59**, 518–535, doi: 10.1111/j.1365-2478.2010.00940.x.

Han, T., A. I. Best, J. Sothcott, and L. M. MacGregor, 2011b, Pressure effects on the joint elastic-electrical properties of reservoir sandstones: Geophysical Prospecting, **59**, 506–517, doi: 10.1111/j.1365-2478.2010.00939.x.

Horby, B. E., 1998, Experimental laboratory determination of the dynamic elastic properties of wet, drained shales: Journal of Geophysical Research, **103**, 29945–29964, doi: 10.1029/97JB02380.

Horne, S., J. Walsh, and D. Miller, 2012, Elastic anisotropy in the Haynesville Shale from dipole sonic data: First Break, **30**, 37–41, doi: 10.3997/1365-2397.2011039.

Jiang, M., and K. T. Spikes, 2013, Estimation of reservoir properties of the Haynesville Shale by using rock-physics modelling and grid searching: Geophysical Journal International, **195**, 315–329, doi: 10.1093/gji/ggt250.

Johansen, T. A., B. O. Ruud, and M. Jakobsen, 2004, Effect of grain scale alignment on seismic anisotropy and reflectivity of shales: Geophysical Prospecting, **52**, 133–149, doi: 10.1046/j.1365-2478.2003.00405.x.

Josh, M., L. Esteban, C. Delle Piane, J. Sarout, D. N. Dewhurst, and M. B. Clenell, 2012, Laboratory characterization of shale properties: Journal of Petroleum Science and Engineering, **88–89**, 107–124, doi: 10.1016/j.petrol.2012.01.023.

Jougnot, D., A. Gorbani, A. Revil, P. Leroy, and P. Consenza, 2010, Spectral induced polarization of partially saturated clay-rocks: A mechanistic approach: Geophysical Journal International, **180**, 210–224, doi: 10.1111/j.1365-246X.2009.04426.x.

Kachanov, M., and I. Sevostianov, 2005, On quantitative characterization of microstructures and effective properties: International Journal of Solids and Structures, **42**, 309–336, doi: 10.1016/j.ijsolstr.2004.06.016.

Kuila, U., 2013, Measurements and interpretation of porosity and pore size distribution in mudrocks: Ph.D thesis, Colorado School of Mines.

Kuila, U., D. K. McCarty, A. Derkowski, T. B. Fischer, and M. Prasad, 2014, Total porosity measurement in gas shales by the water immersion porosimetry (WIP) method: Fuel, **117**, 1115–1129, doi: 10.1016/j.fuel.2013.09.073.

Louis, L., C. David, and P. Robion, 2003, Comparison of the anisotropic behaviour of undeformed sandstones under dry and saturated conditions: Tectonophysics, **370**, 193–212, doi: 10.1016/S0040-1951(03)00186-0.

MacLennan, K., M. Karaoulis, and A. Revil, 2014, Complex conductivity tomography using low-frequency cross-well electromagnetic data: Geophysics, **79**, no. 1, E23–E38, doi: 10.1190/geo2012-0531.1.

Nadri, D., J. Sarout, A. Bóna, and D. Dewhurst, 2012, Estimation of the anisotropy parameters of transversely isotropic shales with a tilted symmetry axis: Geophysical Journal International, **190**, 1197–1203, doi: 10.1111/j.1365-246X.2012.05545.x.

North, L., A. I. Best, J. Sothcott, and L. MacGregor, 2013, Laboratory determination of the full electrical resistivity tensor of heterogeneous carbonate rocks at elevated pressures: Geophysical Prospecting, **61**, 458–470, doi: 10.1111/j.1365-2478.2012.01113.x.

Passey, Q., K. Bohacs, W. Esch, R. Klimentidis, and S. Sinha, 2010, From oil-prone source rock to gas-producing shale reservoir-geologic and petrophysical characterization of unconventional shale gas reservoirs: Presented at International Oil and Gas Conference and Exhibition in China.

Prasad, M., and M. H. Manghnani, 1997, Effects of pore and differential pressures on compressional wave velocity and quality factor on Berea and Michigan sandstones: Geophysics, **62**, 1163–1176, doi: 10.1190/1.1444217.

Prasad, M., K. C. Mba, T. E. McEvoy, and M. L. Batzle, 2011, Maturity and impedance analysis or organic-rich shales: Society of Petroleum Engineers Reservoir Evaluation Engineering, **14**, 533–543.

Revil, A., 2012, Spectral induced polarization of shaly sands: Influence of the electrical double layer: Water Resources Research, **48**, W02517, doi: 10.1029/2011WR011260.

Revil, A., 2013a, Effective conductivity and permittivity of unsaturated porous materials in the frequency range 1 mHz–1 GHz: Water Resources Research, **49**, 306–327, doi: 10.1029/2012WR012700.

Revil, A., 2013b, On charge accumulations in heterogeneous porous materials under the influence of an electrical field: Geophysics, **78**, no. 4, D271–D291, doi: 10.1190/geo2012-0503.1.

Revil, A., W. F. Woodruff, C. Torres-Verdín, and M. Prasad, 2013, Complex conductivity tensor of hydrocarbon-bearing shales: Geophysics, **78**, no. 6, D403–D418, doi: 10.1190/geo2013-0100.1.

Skelt, C., 2011, Haynesville petrophysical analysis, Technical Report, Chevron Energy Technology Company: notes and analysis on proprietary research and petrophysical analyses, unpublished.

Sone, H., and M. D. Zoback, 2013, Mechanical properties of shale-gas reservoir rocks — Part 1: Static and dynamic elastic properties and anisotropy: Geophysics, **78**, no. 5, D381–D392, doi: 10.1190/GEO2013-0050.1.

Sweeney, J. J., J. J. Roberts, and P. E. Harben, 2007, Study of dielectric properties of dry and saturated green river oil shale: Energy and Fuels, **21**, 2769–2777, doi: 10.1021/ef070150w.

Todd, T., and G. Simmons, 1972, Effect of pore pressure on the velocity of compressional waves in low porosity rocks: Journal of Geophysical Research, **77**, 3731–3743, doi: 10.1029/JB077i020p03731.

Vernik, L., and X. Liu, 1997, Velocity anisotropy in shales: A petrophysical study: Geophysics, **62**, 521–532, doi: 10.1190/1.1444162.

Vinegar, H. J., and M. H. Waxman, 1984, Induced polarization of shaly sands: Geophysics, **49**, 1267–1287, doi: 10.1190/1.1441755.

Waxman, M. H., and L. J. M. Smits, 1968, Electrical conductivities in oil bearing shaly sands: SPE Journal, **8**, 107–122, doi: 10.2118/1863-A.

Woodruff, W. F., A. Revil, and C. Torres-Verdin, 2014, Laboratory determination of the complex conductivity tensor of unconventional anisotropic shales: Geophysics, **79**, no. 5, E183–E200, doi: 10.1190/geo2013-0367.1.

Yang, D., and Z. Zang, 2002, Poroelastic wave equation including the Biot/squirt mechanism and the solid/fluid coupling anisotropy: Wave Motion, **35**, 223–245, doi: 10.1016/S0165-2125(01)00106-8.

Zimmermann, E., A. Kemna, J. Berwix, W. Glaas, H. M. Munch, and J. A. Huisman, 2008a, A high-accuracy impedance spectrometer for measuring sediments with low polarizability: Measurement Science and Technology, **19**, 105603, doi: 10.1088/0957-0233/19/10/105603.

Zimmermann, E., A. Kemna, J. Berwix, W. Glaas, and H. Vereeken, 2008b, EIT measurement system with high phase accuracy for the imaging of spectral induced polarization properties of soils and sediments: Measurement Science and Technology, **19**, 094010, doi: 10.1088/0957-0233/19/9/094010.

Zisser, N., A. Kemna, and G. Nover, 2010, Relationship between low frequency electrical properties and hydraulic permeability of low permeability sandstones: Geophysics, **75**, no. 3, E131–E141, doi: 10.1190/1.3413260.

Zisser, N., and G. Nover, 2009, Anisotropy of permeability and complex resistivity of tight sandstones subjected to hydrostatic pressure: Journal of Applied Geophysics, **68**, 356–370, doi: 10.1016/j.jappgeo.2009.02.010.